

# The HST-Gaia Near-Infrared Astrometric Reference Frame near the Milky Way Galactic Center

MATTHEW W. HOSEK JR.,<sup>1,\*</sup> TUAN DO,<sup>1</sup> GREGORY D. MARTINEZ,<sup>1</sup> REBECCA LEWIS-MERRILL,<sup>1</sup> ANDREA M. GHEZ,<sup>1</sup>  
JESSICA R. LU,<sup>2</sup> SHOKO SAKAI,<sup>1</sup> AND JAY ANDERSON<sup>3</sup>

<sup>1</sup>*UCLA Department of Physics and Astronomy, Los Angeles, CA 90095*

<sup>2</sup>*Department of Astronomy, 501 Campbell Hall, University of California, Berkeley, CA, 94720*

<sup>3</sup>*Space Telescope Science Institute, 3700 San Martin Drive, Baltimore, MD 21218, USA*

## ABSTRACT

We present the first high-precision proper motion catalog, tied to the International Celestial Reference System (ICRS), of infrared astrometric reference stars within  $R \leq 25''$  (1 pc) of the central supermassive black hole at the Galactic center (GC). This catalog contains  $\sim 2,900$  sources in a highly extinguished region that is inaccessible via Gaia. New astrometric measurements are extracted from HST observations (14 epochs, 2010 - 2023) and transformed into the ICRS using 40 stars in common with Gaia-DR3. We implement a new method for modeling proper motions via Gaussian Processes that accounts for systematic errors, greatly improving measurement accuracy. Proper motion and position measurements reach precisions of  $\sim 0.03$  mas yr<sup>-1</sup> and  $\sim 0.11$  mas, respectively, representing a factor of  $\sim 20$ x improvement over previous ICRS proper motion catalogs in the region. These measurements define a novel HST-Gaia reference frame that is consistent with Gaia-CRF3 to within 0.025 mas yr<sup>-1</sup> in proper motion and 0.044 mas in position, making it the first ICRS-based reference frame precise enough to probe the distribution of extended mass within the orbits of stars near SgrA\*. In addition, HST-Gaia provides an independent test of the radio measurements of stellar masers that form the basis of current GC reference frames. We find that the HST-Gaia and radio measurements are consistent to within 0.041 mas yr<sup>-1</sup> in proper motion and 0.54 mas in position at 99.7% confidence. Gaia-DR4 is expected to reduce the HST-Gaia reference frame uncertainties by another factor of  $\sim 2$ x, further improving the reference frame for dynamical studies.

*Keywords:* Galactic Center, Astrometry

## 1. INTRODUCTION

The ability to measure stellar motions and orbits at the Milky Way’s Galactic center (GC) allows us to study the central supermassive black hole and surrounding stellar populations at a level of detail not possible for any other galactic nucleus. Nearly 30 years of near-infrared (NIR) high-resolution imaging and spectroscopy of stars in the region have produced a host of groundbreaking discoveries, including the first conclusive evidence that the central source SgrA\* is a supermassive black hole (SMBH; e.g. Schödel et al. 2002; Ghez et al. 2003, 2008; Gillessen et al. 2009), testing the effects of General Relativity near an SMBH such as relativistic redshift (GRAVITY Collaboration et al. 2018; Do et al.

2019) and precession (GRAVITY Collaboration et al. 2020; The GRAVITY Collaboration et al. 2024), and the discovery of young stars in an environment where star formation was thought to be impossible (e.g. Ghez et al. 2003; Paumard et al. 2006; Lu et al. 2009; von Fellenberg et al. 2022; Jia et al. 2023). A foundational component to these studies is the astrometric reference frame, which defines the inertial coordinate system used for the astrometric measurements across these extensive datasets.

An astrometric reference frame is constructed using a set of reference sources with known positions and motions in a well-defined coordinate system on the sky. Constructing a reference frame near the GC is challenging due to the dearth of such reference sources, especially for observations at NIR wavelengths. Quasars and other extragalactic sources, which are commonly used to define reference frames, cannot be observed near the GC in the NIR due to the large amount of extinction along

Corresponding author: Matthew W. Hosek Jr.  
mwhosek@astro.ucla.edu

\* Brinson Prize Fellow

the line-of-sight. The emissive source associated with SgrA\* could serve as a reference source but it is often faint in the NIR and difficult to measure due to source confusion (e.g. Hornstein et al. 2002; Dodds-Eden et al. 2011; Weldon et al. 2023; Pagnat et al. 2024). One solution that has been adopted is to use stellar SiO masers as reference sources near the GC. These masers, which are evolved red giant or supergiant stars with extended atmospheres, are bright sources at both NIR and radio wavelengths. Since SgrA\* is also bright in radio, the positions and motions of the masers can be measured relative to SgrA\* via radio observations. This establishes a reference frame with a coordinate system where SgrA\* is at rest and located at the origin (e.g. Reid et al. 2007; Darling et al. 2023). Since the masers can also be observed in the NIR, they can be used as reference sources to establish the astrometric reference frame for NIR observations (Menten et al. 1997; Reid et al. 2003; Ghez et al. 2008; Gillessen et al. 2009; Yelda et al. 2010; Plewa et al. 2015; Sakai et al. 2019).

However, using SiO masers to define the GC reference frame has its own set of challenges. First, there are a limited number of masers in close proximity of SgrA\*, with only 8 known masers within  $r \lesssim 15''$ . While additional masers can be found at larger radii, the field-of-view (FOV) provided by ground-based NIR observations are restricted due to the technical limitations of the adaptive-optics (AO) corrections required to achieve high-precision astrometry in the region. In addition, the radio emission from an SiO maser originates from an extended circumstellar shell with a typical radius of  $\sim 3 - 6$  AU from the star (e.g. Kemball 2007; Gonidakis et al. 2010). At the GC, such a shell corresponds to an angular size of  $\sim 0.4$  mas –  $0.8$  mas, which is larger than the single-epoch position uncertainty of  $\sim 0.2$  mas that can be achieved by radio observations (Darling et al. 2023). Thus, asymmetries or variability in the shell can cause increased errors (statistical and/or systematic) in the radio astrometry.

The advent of the Gaia satellite has introduced new opportunities to improve the reference frame at the GC. The Gaia-DR3 catalog reports the positions and proper motions of  $\sim 1.5$  billion sources across the sky measured in the Gaia Celestial Reference Frame 3 (Gaia-CRF3; Gaia Collaboration et al. 2022a,b), which is defined by extragalactic sources and ultimately tied to the International Celestial Reference System (ICRS; Arias et al. 1995). As an optical telescope, Gaia does not have the sensitivity required to measure stars at the distance of the GC. However, it can observe foreground stars along the line-of-sight that can serve as a new set of reference sources for the GC NIR reference frame. A chal-

lenge of this approach is that the Gaia stars are located at relatively large projected distances from SgrA\* and generally do not overlap with the ground-based AO observations of stars near the SMBH ( $R \lesssim 25''$ ), and so they cannot be directly used to establish the reference frame for these observations. A recent catalog from the VISTA Variables in the Via Lactea (VVV) survey provides NIR astrometry for stars over a wide area in the Galactic bulge that is tied to Gaia-CRF3 (Griggio et al. 2024), but it is limited in the region surrounding SgrA\* (8 stars within  $R \lesssim 25''$ ) and has proper motion uncertainties of  $\gtrsim 0.7$  mas yr<sup>-1</sup>, which is insufficient for many high-precision science cases at the GC.

We use multiple epochs of Hubble Space Telescope (HST) Wide-Field Camera 3 (WFC3-IR) observations of the GC to bridge the gap between the Gaia reference frame and the AO observations of stars orbiting SgrA\*. HST has the field-of-view necessary to observe enough Gaia stars to accurately define the reference frame as well as the sensitivity and spatial resolution to observe stars at the GC. In this paper, we present a subset of 2876 stars near SgrA\* ( $R \lesssim 25''$ , or  $R \lesssim 1$  pc) with positions and proper motions derived from HST astrometry that has been transformed into Gaia-CRF3. This catalog provides a sample of astrometric reference stars which defines the ‘‘HST-Gaia reference frame’’ which, unlike past maser-based GC reference frames, is in the ICRS coordinate system. A key advantage of HST-Gaia over maser-based reference frames is that there are significantly more Gaia stars than masers available to define the coordinate system. In addition, it is the first GC NIR reference frame that is independent of the radio maser measurements, enabling tests for systematics in maser-based reference frames.

This paper is organized as follows. The HST observations and measurements are described in §2. The methodology for transforming the HST astrometry into the Gaia-CRF3 reference frame and deriving stellar proper motions is described §3. The proper motion catalog of the sample highlighted in this paper is presented in §4, along with an analysis of the consistency between the HST-Gaia and radio measurements for stellar maser near SgrA\*. The uncertainties in the HST-Gaia reference frame are compared to previous GC NIR reference frames, applications of the HST-Gaia reference frame to GC science, and the expected improvement in the HST-Gaia reference frame with Gaia-DR4 are discussed in §5. Finally, our conclusions are summarized in §6.

## 2. HST OBSERVATIONS AND MEASUREMENTS

Multiple epochs of observations of a  $2' \times 2'$  region centered on SgrA\* ( $\alpha(\text{J2000}) = 17^{\text{h}}45^{\text{m}}40.04^{\text{s}}$ ,  $\delta(\text{J2000}) =$

-29°00′28″.10) were obtained with the the HST WFC3-IR channel between 2010.6261 – 2023.6178 (Figure 1). This dataset contains 14 epochs of observations in the F153M filter for the purpose of measuring proper motions and a single epoch of observations in the F127M and F139M filters to measure stellar colors. The F153M observations were taken over a span of different HST General Observer (GO) programs and thus have different depths and position angles (PAs). A summary of the observations is provided in Table 1, all of which can be found in the Barbara A. Mikulski Archive for Space Telescopes (MAST)<sup>1</sup>.

Stellar astrometry and photometry are extracted for each epoch using the same procedure described in Hosek et al. (2022) and references therein. Initial detection and measurement of stars in each image are obtained by the FORTRAN routine `img2xym_wfc3ir` (a precursor to the package `hst1pass` described in Anderson 2022). The stars are fit using a library of spatially-variable PSFs for the appropriate filter, which are arranged in a 3 x 3 grid that spans the field. The star images in each exposure are compared to the library PSFs and a uniform perturbation to the PSFs is applied to minimize the PSF residuals. A second round of measurements is then performed using the perturbed PSFs to produce a starlist containing star positions and magnitudes. The starlists for the individual images within each epoch are transformed into a common reference frame using a first-order polynomial transformation (three free parameters per dimension) based on the pixel positions of common stars.

A final combined starlist is created for each epoch from the average astrometry and photometry across the individual images within that epoch. This is done using the FORTRAN routine `KS2` (Anderson et al. 2008; Bellini et al. 2017, 2018). `KS2` uses the transformations derived from the initial starlists to combine the images within the epoch into a single average image. Stars are detected in the average image, where fainter stars can be detected compared to the individual images alone. Astrometric and photometric measurements of each star are then made in the individual images with the neighboring stars subtracted, and then the average positions and fluxes are computed for each epoch.

The astrometric error of each star is taken to be the error-on-the-mean of its positions measured in all images within an epoch ( $\sigma_{HST} = \sigma_{img} / \sqrt{N_{img}}$ , where  $\sigma_{HST}$  is the astrometric error and  $\sigma_{img}$  is the standard deviation of the positions across  $N_{img}$ ). The intrinsic

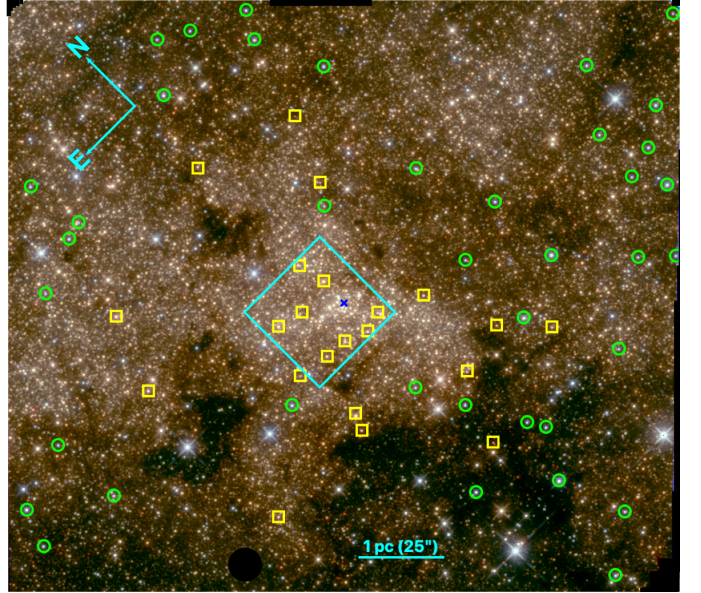


**Figure 1.** The HST WFC3-IR field (red = F153M, green = F139M, blue = F127M), which is approximately centered on SgrA\* (blue cross). The HST astrometry is transformed into Gaia-CRF3 using 40 primary reference stars found in the Gaia-DR3 catalog (green circles). We report HST-Gaia positions and proper motions for these sources as well as for 2823 secondary reference stars located in a 22''x22'' region that overlaps ground-based AO observations of the GC (cyan box; Sakai et al. 2019) and for 13 stellar masers found in the field (yellow squares).

photometric error is taken to be the standard deviation of the instrumental magnitudes measured across the images, which was found to more accurately reflect the true photometric scatter than the error-on-the-mean (Hosek et al. 2015). The instrumental magnitudes are converted into Vega magnitudes using the `KS2` zeropoints from Hosek et al. (2018), and the error on the zeropoints ( $\sim 0.01$  mags) is added in quadrature with the intrinsic photometric error. The final starlists typically contain  $\sim 50,000$  stars measured in each epoch of the F153M observations and  $\sim 40,000$  stars measured in the F127M and F139M observations across the full HST field. Note that in this paper we will mainly focus on sources within  $R \leq 25''$  (1 pc) of SgrA\*; the measurements across the entire field will be presented in future work (Hosek et al., in prep).

### 3. HST-GAIA PROPER MOTIONS

We measure stellar proper motions by transforming each epoch of HST observations into the Gaia-CRF3 reference frame (Gaia Collaboration et al. 2022a). These transformations are calculated using stars in common between HST and Gaia-DR3. We refer to these as the

<sup>1</sup> 10.17909/vre6-c497

**Table 1.** HST WFC3-IR Observations

Date (Year)	Program ID/PI	Filter	PA (deg)	$N_{img}$	$t_{img}$ (s)	$t_{tot}$ (s)	Used for Astrometry?
2010.6261	11671/Ghez	F127M	-45.3	12	599.23	7190	False
2010.6258	11671/Ghez	F139M	-45.3	10	349.23	3492	False
2010.4918	11671/Ghez	F153M	-45.3	21	349.23	7333	True
2011.6863	12318/Ghez	F153M	-45.3	21	349.23	7333	True
2012.6052	12667/Ghez	F153M	-45.3	21	349.23	7333	True
2014.099	13049/Do	F153M	134.7	4	249.23	997	True
2018.1064	15199/Do	F153M	134.7	16	349.23	5538	True
2019.162	15498/Do	F153M	134.7	16	349.23	5538	True
2019.6701	16004/Do	F153M	-45.3	27	349.23	9429.3	True
2019.7046	16004/Do	F153M	-45.3	27	349.23	9429.3	True
2019.7924	16004/Do	F153M	-45.3	27	349.23	9429.3	True
2020.2234	15894/Do	F153M	134.7	20	349.23	6985	True
2022.1428	16681/Do	F153M	134.7	21	299.23	6284	True
2022.5441	16681/Do	F153M	-45.3	21	299.23	6284	True
2023.1535	16990/Do	F153M	134.7	21	299.23	6284	True
2023.6178	16990/Do	F153M	-45.3	21	299.23	6284	True

NOTE—Description of columns. Date: average date of observations (calculated assuming the Gregorian calendar), Program ID/PI: HST program ID and PI, Filter: filter, PA: position angle,  $N_{img}$ : number of images,  $t_{img}$ : integration time per image;  $t_{tot}$ : total integration time.

primary reference stars, which are identified in §3.1. Stellar proper motions are then measured using a new method that utilizes Gaussian Processes to model systematic errors as described in §3.2. We refer to these measurements as the HST-Gaia proper motions. The consistency between the HST-Gaia reference frame established by these measurements and Gaia-CRF3 is then assessed in §3.3.

The Gaia-CRF3 reference frame is a realization of the ICRS, which defines a coordinate system that is defined relative to extragalactic objects with no proper motion (Arias et al. 1995). By extension, the HST-Gaia proper motions are in the ICRS coordinate system as well. However, for some applications it is useful to measure stellar proper motions in a coordinate system where SgrA\* is at the origin and has no proper motion<sup>2</sup>, which we refer to as SgrA\*-at-Rest coordinates. We discuss how to convert the HST-Gaia proper motions into SgrA\*-at-Rest coordinates in §3.4. We refer to these as the SgrA\*-at-Rest proper motions.

### 3.1. Transforming HST Astrometry into the Gaia-CRF3 Reference Frame

<sup>2</sup> Note that in SgrA\* has a non-zero proper motion in the ICRS due to the reflex motion of the Sun’s orbit around the Galaxy. This motion is defined observationally.

The HST astrometry is transformed into the Gaia-CRF3 reference frame using a set of primary reference stars that are well-measured in both the HST and Gaia-DR3 catalogs. However, there are a limited number of such sources available. Due to the high extinction near the GC ( $A_{K_s} \sim 2.7$  mag; Schödel et al. 2010), most of the NIR sources detected by HST are too faint at optical wavelengths to be detected by Gaia. On the other hand, sources detected by Gaia must come from the less-extinguished foreground population and may be saturated in the HST data. In addition, the high stellar crowding in the field can bias the astrometric measurements of either Gaia or HST. Thus, the selection of the primary reference stars must be made with care.

To begin, we make a series of quality cuts to the Gaia-DR3 catalog to identify Gaia sources in the region with reliable astrometry (Arenou et al. 2018; Lindegren et al. 2021; Fabricius et al. 2021). We consider Gaia-DR3 stars with the following catalog values:

- `astrometric_params_solved = 31`, indicating that the source has a five-parameter astrometric solution (position, parallax, and proper motion) and that accurate color-dependent PSF correction terms can be applied
- `duplicated_source = False`, which requires that no other *Gaia* source is detected within  $0.''18$

- `parallax_over_error`  $\geq -10$ , eliminating sources with significantly unphysical parallaxes
- `astrometric_excess_noise_sig`  $\leq 2$ , removing sources with significant excess noise in the Gaia astrometric solution beyond the statistical errors
- `RUWE`  $\leq 1.4$ , also to remove sources with significant excess noise relative to the Gaia astrometric solution
- `phot_g_mean_mag`  $> 13$  mag, to avoid additional systematic errors in the Gaia astrometry for bright sources

There are 55 Gaia-DR3 stars that overlap with the HST field after these cuts. The positions of the Gaia stars are converted into angular offsets from a fiducial position near the center of the HST field, chosen to be  $(\alpha_f(\text{ICRS}), \delta_f(\text{ICRS})) = (17^h 45^m 40.032863^s, -29^\circ 00' 28''.24260)$ . These offsets are denoted as  $\delta_{\alpha*} = (\alpha - \alpha_f)\cos(\delta)$  and  $\delta_\delta = (\delta - \delta_f)$ .

The final set of primary reference stars is selected using an iterative process. First, the positions of the Gaia stars at each HST epoch are calculated using the Gaia-DR3 proper motions, with the uncertainties in the Gaia positions calculated via the propagation of Gaia catalog errors. Then, the Gaia stars are matched to HST sources, and Gaia stars with corresponding HST sources with  $F153M \leq 13$  mag are removed as a conservative limit to avoid saturation in the HST image. This eliminates 5 Gaia stars from the sample. Next, the remaining Gaia stars are used to calculate a second-order polynomial via linear least squares minimization to transform HST pixel coordinates  $(x, y)$  into Gaia-CRF3 coordinates  $(\delta_{\alpha*}, \delta_\delta)$ :

$$\delta_{\alpha*} = a_0 + a_1x + a_2y + a_3xy + a_4x^2 + a_5y^2 \quad (1)$$

$$\delta_\delta = b_0 + b_1x + b_2y + b_3xy + b_4x^2 + b_5y^2 \quad (2)$$

where  $\{a_0, a_1, \dots, b_0, b_1, \dots\}$  are the coefficients of the polynomials. A second-order polynomial is used because it was found to be the most effective as reducing the residuals to the fit. Testing revealed that a first-order polynomial resulted in statistically significant position residuals for many of the reference stars, while a third-order polynomial did not offer a noticeable improvement over the second-order polynomial.

Next, the uncertainty in the transformation ( $\sigma_{trans}$ ) is characterized using a full sample bootstrap over the reference stars. For each epoch, the reference stars are resampled with replacement for 100 iterations. The transformations are recalculated for each iteration and applied to HST astrometry. For each star, the standard

deviation of the transformed positions across the iterations is taken to be  $\sigma_{trans}$  for that star. The total astrometric error ( $\sigma_{ast}$ ) for a star in a given epoch is then calculated as:

$$\sigma_{ast} = \sqrt{\sigma_{HST}^2 + \sigma_{trans}^2} \quad (3)$$

where  $\sigma_{HST}$  is the astrometric error of the HST measurements (see §2). The HST-Gaia proper motions of the stars are then calculated from the transformed HST astrometry and corresponding  $\sigma_{ast}$  values using the methodology described in §3.2.

Lastly, the sample of Gaia reference stars is examined for outliers by comparing their HST-Gaia proper motions to their original values from the Gaia-DR3 catalog. Reference stars with either position or proper motion differences larger than  $5\sigma$  (where  $\sigma$  is the quadratic sum of the HST-Gaia and Gaia-DR3 errors) are considered outliers. This conservative threshold is adopted to identify the strongest outliers in the sample, which would have undue influence on the transformation parameters. If one or more outliers are present, then the largest outlier is eliminated from the reference star sample and the process is repeated. These iterations continue until no outliers are found to exist, which was achieved after 10 Gaia stars are eliminated from the primary reference star sample. Many of the Gaia stars removed in this manner were found to either lie within several pixels of the edge of the HST field (visibly truncating their PSF) or be in close proximity to neighboring stars, compromising their HST astrometry.

The final set of primary reference stars used to transform the HST astrometry into the Gaia-CRF3 reference frame is comprised of 40 sources. These stars span a range of Gaia magnitudes between  $15.1 \text{ mag} < G < 20.2 \text{ mag}$  and have a median position error of 0.15 mas and a median proper motion error of  $0.16 \text{ mas yr}^{-1}$  in the Gaia DR3 catalog (Table 2). The average  $\sigma_{trans}$  achieved by the resulting transformations varies between 0.2 – 0.5 mas depending on the epoch (Figure 2). The fact that  $\sigma_{trans}$  generally increases as the time from the Gaia-DR3 reference epoch (2016.0) increases indicates that the transformation errors are limited by the Gaia-DR3 measurement errors for the reference stars. Figure 2 also shows how  $\sigma_{trans}$  varies as a function of position in the HST field, with increasing error towards the field edges and in regions where there are fewer Gaia reference stars nearby.

### 3.2. Modeling Proper Motion Systematics using Gaussian Processes

Systematic errors can introduce correlations between astrometric measurements that are not related to the

**Table 2.** Primary Reference Stars: Gaia DR3 Catalog Measurements

source_id	phot_g_mean_mag	ra	ra_error	dec	dec_error	pmra	pmra_error	pmdec	pmdec_error
	(mag)	(deg)	(mas)	(deg)	(mas)	(mas/yr)	(mas/yr)	(mas/yr)	(mas/yr)
4057481683573622528	18.24	266.39940889	0.173	-29.01953897	0.138	2.050	0.202	-4.857	0.130
4057481683573626880	15.88	266.39651474	0.043	-29.01633561	0.033	0.263	0.049	-2.250	0.031
4057481717933348608	17.39	266.41697834	0.101	-29.02998491	0.080	-6.113	0.118	-5.658	0.073
4057481717933350528	17.99	266.41359224	0.149	-29.02779105	0.120	-7.100	0.173	-5.444	0.108
4057481717933358848	17.25	266.41955472	0.094	-29.02096452	0.072	1.789	0.110	0.788	0.066
4057481717933359360	18.04	266.41333717	0.147	-29.02119722	0.119	0.019	0.174	-5.168	0.111
4057481717934037760	19.12	266.41807115	0.326	-29.03107056	0.258	3.333	0.371	1.031	0.229
4057481717938509312	18.59	266.41397518	0.198	-29.02023107	0.159	-1.315	0.246	-3.164	0.152
4057481722235384320	15.12	266.41521387	0.029	-29.02387599	0.024	-0.223	0.036	-1.737	0.022
4057481722235386368	18.56	266.41602804	0.201	-29.01701274	0.158	1.363	0.239	2.421	0.147

NOTE—Columns are as defined in the Gaia DR3 source catalog. All positions are at the Gaia DR3 reference epoch of 2016.0.

NOTE—This table is available in its entirety in the machine-readable format.

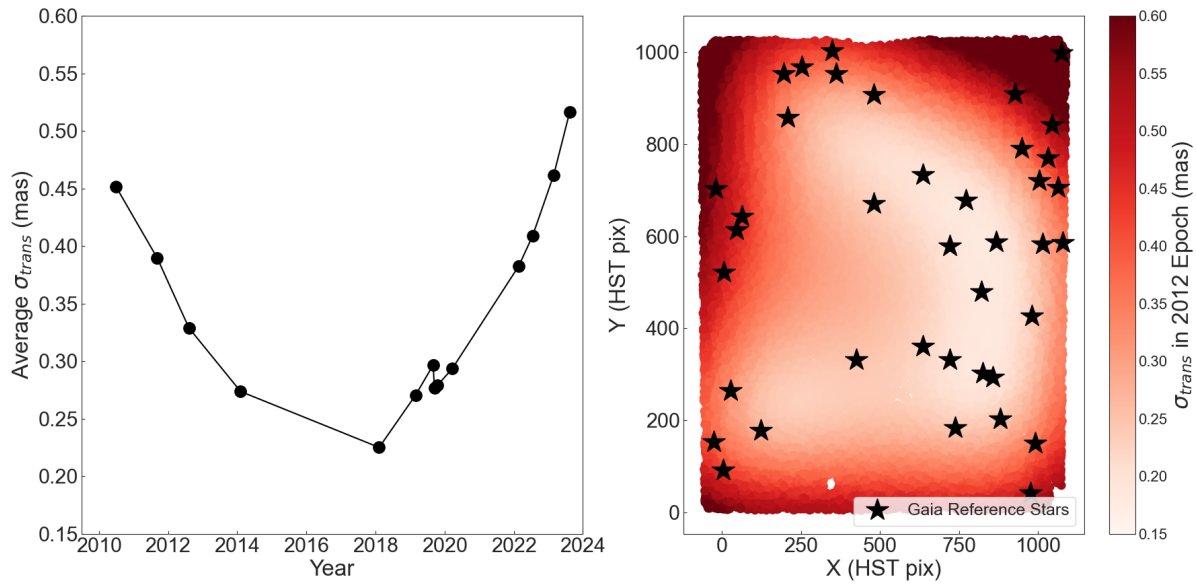


**Figure 2.** The transformation errors ( $\sigma_{trans}$ ) for the HST-Gaia astrometry, which varies as a function of time and position. Left: Average  $\sigma_{trans}$  as a function of time, which generally increases as the time from the Gaia-DR3 reference epoch (2016) increases. Right:  $\sigma_{trans}$  as a function of position on the HST detector for the 2012 epoch (pixel scale =  $1.21'' \text{ pix}^{-1}$ ), with the positions of the Gaia reference stars shown by black stars.  $\sigma_{trans}$  generally increases near the edges of the field as well as in areas with fewer reference stars.

proper motion of a given source. Possible sources of systematic errors include stellar crowding, where a neighboring star moves close enough to a given star to bias its astrometry (e.g. Jia et al. 2019), and shifts in the astrometric reference frame, which would introduce correlated astrometric residuals as a function of time. We find an additional systematic in the HST astrometry that causes the star positions to shift depending on the position angle (PA) of the observations. The size of the position shift increases with magnitude, reaching as large

as  $\sim 2$  mas for faint stars (see Appendix A). These systematic error must be addressed in order to accurately measure proper motions.

We introduce a new approach to model proper motions in the presence of such systematics. We utilize Gaussian Processes (Rasmussen & Williams 2006) to simultaneously fit stellar proper motion and systematic correlations. These models use one or more kernels (see Appendix B):

- *Polynomial kernel* ( $K^{(\text{poly})}$ ): Fits the motion of the star as a function of time with a polynomial. We use a first-order polynomial to measure the linear proper motion of a star:

$$x' = x_0 + \mu_x(t - t_0) \quad (4)$$

where  $x'$  is the observed position at time  $t$  (i.e. either  $\delta_{\alpha^*}$  or  $\delta_\delta$ ),  $x_0$  is the  $x$  position at  $t_0$ ,  $\mu_x$  is the proper motion, and  $t_0$  is the astrometric-error weighted average time across the data (Appendices B.1, B.2).

- *Squared-exponential kernel* ( $K^{(\text{sqexp})}$ ): Models time-correlated data using a squared-exponential function. We use this to model systematics that are induced by shifts in the astrometric reference frame or observing PA (Appendix B.3).
- *Step kernel* ( $K^{(\text{step})}$ ): Models time-correlated data using a step function. We use this as an alternative kernel to capture systematics induced by shifts in the astrometric reference frame or observing PA (Appendix B.3).
- *Confusion kernel* ( $K^{(\text{conf})}$ ): Models systematics correlated with spatial position, such as biases induced by stellar confusion with a nearby source (Appendix B.4).

In addition, an additive error can be included in the model which inflates the measurement uncertainties for each data point by a constant value. This is useful in the case where the measurement uncertainties are systematically underestimated.

Before applying these kinematic models to derive stellar proper motions, we remove severe astrometric outliers from the data via leave-one-out (LOO) cross-validation (e.g. Vehtari et al. 2015; Do et al. 2019, see also Appendix B.6). Such outliers can be caused by cases of incorrect source matching between epochs or significant stellar confusion. For each star, we fit an initial kinematic model comprised of only the polynomial kernel to the data (the  $\alpha^*$  and  $\delta$  positions are fit independently). If the difference between an observed data point and its predicted value from a fit with that point removed (i.e., the LOO prediction) is greater than 5x the uncertainty in the LOO prediction in either  $\alpha^*$  or  $\delta$ , then that data point is identified as an outlier and removed (e.g. a  $5\sigma$  outlier cut, as a conservative threshold for identifying outliers). This process removes  $\sim 5.5\%$  of the total number of HST astrometric measurements from the sample.

After outlier rejection, proper motions are derived for all stars that have at least 3 epochs of F153M astrometry. In cases where there are  $\leq 4$  epochs of astrometry,

then there aren't enough data to constrain the kinematic models with additional kernels beyond the polynomial kernel (since each kernel has 2 free parameters). Instead, linear regression is used to fit the proper motions according to Equation 4. For sources with  $\geq 5$  epochs of astrometry, several kinematic models are fit to the data:

- *poly-only*: polynomial kernel ( $K^{(\text{poly})}$ ) only
- *poly+sqexp*: polynomial kernel ( $K^{(\text{poly})}$ ) plus the squared-exponential kernel ( $K^{(\text{sqexp})}$ ).
- *poly+step*: polynomial kernel ( $K^{(\text{poly})}$ ) plus the step kernel ( $K^{(\text{step})}$ ).
- *poly+confusion*: polynomial kernel ( $K^{(\text{poly})}$ ) plus the confusion kernel ( $K^{(\text{conf})}$ )
- *poly+add*: polynomial kernel ( $K^{(\text{poly})}$ ) plus an additive error

For the sample reported in this paper, only one star has  $\leq 4$  epochs of astrometry and is fit using linear regression while the rest have  $\geq 5$  epochs and are fit using these kinematics models.

We use the Expected Log Probability Distribution (ELPD; see Vehtari et al. 2016; Gelman et al. 2013) to determine which kinematic model is preferred:

$$\text{ELPD} = \sum_i^N \log(P(x_i | \mathbf{x}_{-i})) \quad (5)$$

where  $P(x_i | \mathbf{x}_{-i})$  is the probability of observing the  $i$ -th data point given the model that excludes this data point and  $N$  is the number of data points in the fit. If the model is a Gaussian Process then  $x_i$  is distributed normally:

$$x_i \sim \mathcal{N}(x_{100_i}, \sigma_{100_i}^2) \quad (6)$$

where  $x_i$  is the observed value of the  $i$ -th data point,  $x_{100_i}$  is the LOO prediction for the value of that data point, and  $\sigma_{100_i}^2$  is the variance of the LOO prediction, which (see Appendix B.6). Thus:

$$P(x_i | \mathbf{x}_{-i}) = \frac{1}{\sqrt{2\pi\sigma_{100_i}^2}} \exp\left[-\frac{(x_i - x_{100_i})^2}{2\sigma_{100_i}^2}\right] \quad (7)$$

The ELPD is calculated for the  $\alpha^*$  and  $\delta$  fits and then are summed together to calculate the total ELPD for a given model of a given star. Note that the ELPD will favor a model that best describes the variance in the data (i.e., minimizes  $x_i - x_{100_i}$  relative to  $\sigma_{100_i}^2$ ) with the lowest possible LOO uncertainties possible. Further, the ELPD penalizes models that overfit the data through the use of the LOO prediction: for overfit models,  $x_i - x_{100_i}$

(hereafter referred to as the LOO residual) will be large, since the removal of a given data point will significantly change the model.

We accept a model with two kernels over the single-kernel *poly-only* model if the ELPD of the two-kernel model is greater by  $\geq 6$ . This criterion implies that the probability of the *poly-only* model being preferred over the two-kernel model is  $\sim 0.0025$ , *e.g.*, the two-kernel model is preferred at the  $\sim 3\sigma$  probability level. If this threshold is met, then we conclude that the additional free parameters introduced by the two-kernel model are necessary. The two-kernel model with the highest ELPD (i.e. the highest probability) is then adopted as the preferred model. An example where the *poly+sqexp* model is identified as the preferred model is shown in Figure 3.

### 3.2.1. Assessing the Best-Fit Kinematic Models

Ideally, the best-fit kinematic model for a given star would provide LOO predictions for the data that are consistent with the observed values within the LOO uncertainties. To test this, we define a metric similar to the reduced chi-squared:

$$\widetilde{\chi_{\text{loo}}^2} = \frac{\chi_{\text{loo}}^2}{N}, \quad (8)$$

where  $N$  is the number of astrometric measurements and

$$\chi_{\text{loo}}^2 = \sum_{i=1}^{i=N} \frac{(x_i - x_{\text{loo}_i})^2}{\sigma_{\text{loo}_i}^2} \quad (9)$$

where  $x_i$  is the observed star position at the  $i$ th of  $N$  astrometric epochs,  $x_{\text{loo}_i}$  is the LOO prediction for the star position from the kinematic model at that epoch, and  $\sigma_{\text{loo}_i}$  is the uncertainty of the LOO prediction (see Appendix B.6). This metric provides a measure of the size of the LOO residual for each epoch relative to the LOO uncertainty at that epoch.

For the sample of stars presented in this paper, we calculate the expected distribution of  $\widetilde{\chi_{\text{loo}}^2}$  in the ideal case where the LOO residual are indeed consistent with the LOO uncertainty at each data point. First, we assume that the LOO predictions from the best-fit kinematic models represent the true positions of the stars at each of the HST epochs. Each position is then perturbed by the measurement uncertainty (i.e., modified by a random value drawn from a Gaussian distribution with a mean of zero and a standard deviation equal to the observed astrometric error from Equation 3) to represent a measurement of that star position. The resulting  $\widetilde{\chi_{\text{loo}}^2}$  distribution across the predicted measurements is then calculated. This process is repeated 1000 times to calculate the average expected distribution for  $\widetilde{\chi_{\text{loo}}^2}$  for the sample.

If the best-fit kinematic models provide a good description of the data, then the observed distribution of  $\widetilde{\chi_{\text{loo}}^2}$  would be similar to the expected distribution of  $\chi_{\text{loo}}^2$  for the sample. This comparison is shown in Figure 4. We find that the peaks of the observed and expected  $\widetilde{\chi_{\text{loo}}^2}$  distributions are indeed quite similar, with the observed distribution being somewhat narrower than expected. On the other hand, if *poly-only* models are used for all of the stars, then the resulting  $\widetilde{\chi_{\text{loo}}^2}$  distribution is significantly broader than the expected distribution. This indicates that the observed LOO residuals are generally larger than the uncertainty in the *poly-only* models, suggesting that there are systematic correlations in the astrometry that are not captured when only the *poly-only* models are used. In contrast, the best-fit kinematic models better capture these correlations and generally provide good fits to the data.

### 3.3. The HST-Gaia Reference Frame: Consistency with Gaia-CRF3

The HST-Gaia measurements define the ‘‘HST-Gaia reference frame’’, i.e., a reference frame defined by HST measurements that are transformed into Gaia-CRF3. The transformation errors ( $\sigma_{\text{trans}}$ ) calculated in §3.1 quantify the statistical error in the transformation into the Gaia-CRF3 reference frame (e.g., due to the precision of the reference star measurements) as well as systematic errors that may be present between the reference stars themselves (e.g., if a particular reference star is biased relative to the rest of the sample). Here we assess the overall consistency between the HST-Gaia and Gaia-CRF3 coordinate systems. A discrepancy would result in an average systematic bias between the HST-Gaia and Gaia-DR3 measurements of the primary reference stars. The size and uncertainty of this bias represents the highest possible accuracy and precision of measurements in the HST-Gaia reference frame relative to the Gaia-CRF3 coordinate system.

We define the bias between the HST-Gaia and Gaia-CRF3 reference frames as the error-weighted mean difference between the positions and proper motion values for the primary reference stars:

$$\Delta x = \frac{\sum_i^N w_i (x_{i,\text{HST-Gaia}} - x_{i,\text{DR3}})}{\sum_i^N w_i} \quad (10)$$

where  $x_{i,\text{HST-Gaia}}$  and  $x_{i,\text{DR3}}$  are the HST-Gaia and Gaia-DR3 values for the  $i$ th reference star, respectively, and the weight  $w_i = 1/\sigma_i^2$ , where  $\sigma_i$  is the quadratic sum of the associated HST-Gaia and Gaia-DR3 errors on those values. The uncertainty in the bias is then the

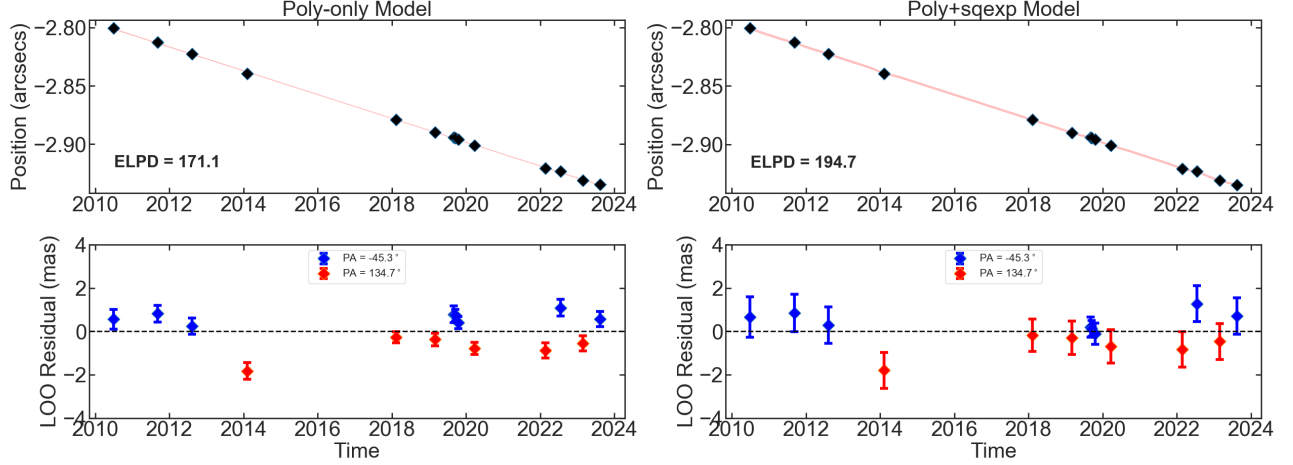


**Figure 3.** An example application of the new kinematic models introduced in this paper to the proper motion of the star S3-374. The left panel shows the *poly-only* model fit while the right panel show the *poly+sqexp* model fit. For each panel, the top plot shows the model (red, with the shaded region showing the uncertainty) compared to the observed data (black points), with the corresponding ELPD of the model printed to the lower left of the plot. The bottom plot in each panel shows the LOO residuals between the model and data, where the color of each data point corresponds to the PA of the epoch and the errorbars represent the LOO uncertainty at each point. The *poly-only* model shows correlated residuals due to the changing PA of the observations (see Appendix A), which produces a larger variance in the data than can be explained by the model. These residuals are reduced and better captured by the uncertainty in the *poly+sqexp* model, which is strongly preferred by the ELPD.

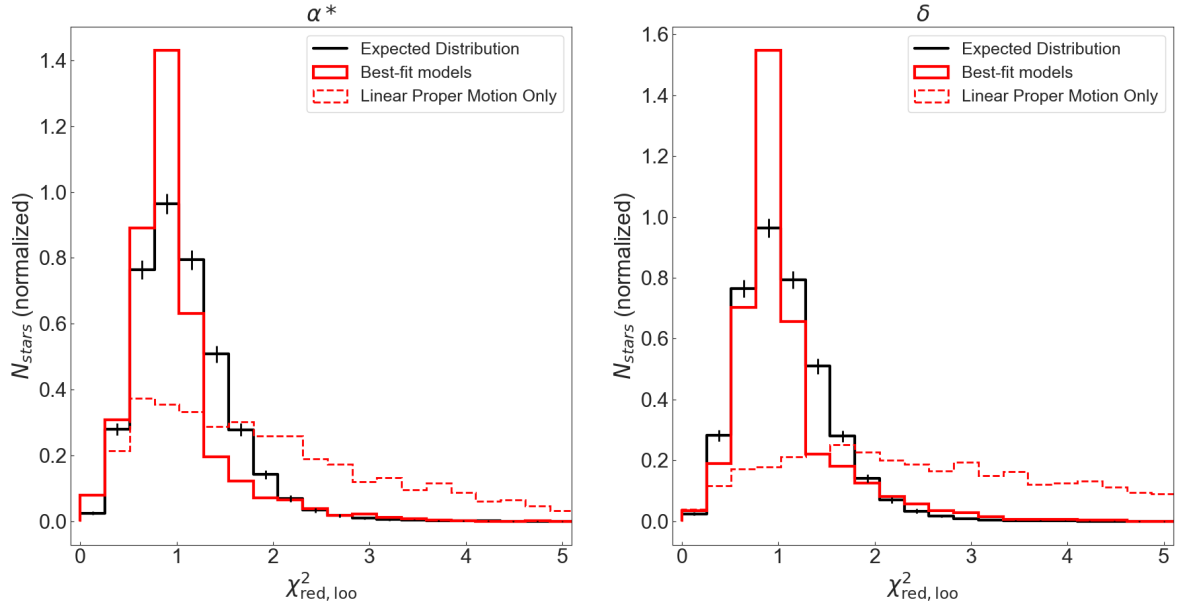


**Figure 4.** The observed and expected distributions of  $\widetilde{\chi^2_{\text{loo}}}$  for the astrometric reference stars presented in this paper, with  $\alpha^*$  on the left and  $\delta$  on the right. In both cases, the observed distribution of the best-fit kinematic models (solid red histograms) peak at similar values as the expected distributions (black histograms). However, if *poly-only* models used for all stars, then the resulting distribution of  $\widetilde{\chi^2_{\text{loo}}}$  extends to significantly higher values than expected due to systematic errors in the astrometry beyond what the *poly-only* models can capture (red dashed histograms).

error on the weighted mean:

$$\sigma_{\Delta x} = \frac{1}{\sqrt{\sum_i^N w_i}} \quad (11)$$

Calculating the proper motion bias between the HST-Gaia and Gaia-DR3 measurements is straightforward since the proper motions can simply be subtracted to find the difference. In order to calculate the position bias we must first use the HST-Gaia and Gaia-DR3 proper motions to infer the positions of the reference stars at a common epoch. This epoch ( $t_{0,comp}$ ) is chosen to be the error-weighted average reference epoch of the proper motion measurements:

$$t_{0,comp} = \frac{\sum_i^N \sigma_{H,i}^2 t_{0,H,i} + \sigma_{G,i}^2 t_{0,G,i}}{\sum_i^N \sigma_{H,i}^2 + \sigma_{G,i}^2} \quad (12)$$

where  $\sigma_{H,i}$  is the HST-Gaia proper motion error for the  $i$ th star,  $t_{0,H,i}$  is the HST-Gaia reference epoch for the  $i$ th star, and  $\sigma_{G,i}$  and  $t_{0,G,i}$  are the analogous values for the Gaia proper motion of the  $i$ th star. This represents the time at which the uncertainty in the difference between the HST and Gaia positions is minimized (e.g. Yelda et al. 2010), which is calculated to be 2016.0605 for this sample. Then, Equations 10 and 11 can be applied using the inferred positions at  $t_{0,comp}$ .

The differences between the HST-Gaia and Gaia-CRF3 position and proper motion measurements for the primary reference stars are shown in Figure 5. For the proper motions, we derive the bias to be  $\Delta\mu_{\alpha^*} = -0.015 \pm 0.020$  mas yr<sup>-1</sup> and  $\Delta\mu_{\delta} = 0.002 \pm 0.015$  mas yr<sup>-1</sup>. This indicates that there is no evidence for a bias between the HST-Gaia and Gaia-CRF3 proper motions to a total precision of  $\sigma_{\Delta pm} = \sqrt{\sigma_{\Delta\mu_{\alpha^*}}^2 + \sigma_{\Delta\mu_{\delta}}^2} = 0.025$  mas yr<sup>-1</sup>. For the positions, we find  $(\Delta\delta_{\alpha^*}, \Delta\delta_{\delta}) = (-0.007 \pm 0.032, -0.030 \pm 0.030)$  mas, indicating that there is no evidence for a bias between HST-Gaia and Gaia-DR3 positions to a total precision of  $\sigma_{\Delta pos} = \sqrt{\sigma_{\Delta\delta_{\alpha^*}}^2 + \sigma_{\Delta\delta_{\delta}}^2} = 0.044$  mas.

### 3.4. Transforming the HST-Gaia Proper Motions Into SgrA\*-at-Rest Coordinates

We convert the HST-Gaia measurements from ICRS coordinates into SgrA\*-at-Rest coordinates using the ICRS position and proper motion of SgrA\* measured by Xu et al. (2022)<sup>3</sup>. The SgrA\*-at-Rest proper motions

( $\mu_{\alpha^*}^s, \mu_{\delta}^s$ ) are calculated by subtracting the SgrA\* ICRS proper motion from the HST-Gaia proper motions:

$$\mu_{\alpha^*}^s = \mu_{\alpha^*} - \mu_{\alpha^*,sgra} \quad (13)$$

$$\mu_{\delta}^s = \mu_{\delta} - \mu_{\delta,sgra} \quad (14)$$

where  $\mu_{\alpha^*,sgra}, \mu_{\delta,sgra}$  is the SgrA\* ICRS proper motion from Xu et al. (2022). Calculating the SgrA\*-at-Rest positions requires multiple steps since the ICRS position of SgrA\* changes with time. For each star, we first use the Xu et al. (2022) proper motion to calculate the ICRS position of SgrA\* at the reference epoch of that star's HST-Gaia proper motion fit (i.e.,  $t_0$  in Equation 4). We denote this position as  $(\alpha_{sgra}(t_0), \delta_{sgra}(t_0))$ . Next, we calculate the offset between this position and the fiducial position of the HST-Gaia measurements:

$$d\alpha^* = (\alpha_{sgra}(t_0) - \alpha_f) * \cos(\delta_{sgra}) \quad (15)$$

$$d\delta = \delta_{sgra}(t_0) - \delta_f \quad (16)$$

Then, these offsets are subtracted from the reference epoch position of the HST-Gaia proper motion fit to get the star's position relative to SgrA\* at the reference epoch, denoted  $\delta_{\alpha_0}^s$  and  $\delta_{\delta_0}^s$ :

$$\delta_{\alpha_0}^s = \delta_{\alpha^*0} - d\alpha^* \quad (17)$$

$$\delta_{\delta_0}^s = \delta_{\delta_0} - d\delta \quad (18)$$

We justify adopting the SgrA\* ICRS measurements from Xu et al. (2022) over others in the literature (e.g. Reid & Brunthaler 2020; Gordon et al. 2023) in Appendix C.

## 4. RESULTS

### 4.1. A Catalog of HST-Gaia Stars Within the Central Parsec of the Galaxy

We present a proper motion catalog of 2876 stars derived from the HST-Gaia measurements which represent astrometric reference stars for the HST-Gaia reference frame within  $R \leq 25''$  (1 pc) of SgrA\*. The process used to identify these stars is described in §4.1.1. The sample can be separated into 3 groups. The first group is the 40 Gaia reference stars that are used to transform the HST astrometry into the Gaia-CRF3 reference frame. We refer to these as the primary reference stars since they define the HST-Gaia coordinate system. The second group contains 2823 well-measured stars within  $R \lesssim 25''$  that fall within footprint of ground-based AO imaging of the GC (e.g. Plewa et al. 2015; Sakai et al. 2019). These are the secondary reference stars which establish the HST-Gaia reference frame in this region. The third group is 13 stellar masers which overlap with

<sup>3</sup> Xu et al. (2022) measure the position of SgrA\* to be  $\alpha(\text{J2000}) = 17^{\text{h}}45^{\text{m}}40^{\text{s}}.032863 \pm 0^{\text{s}}.000016$ ,  $\delta(\text{J2000}) = -29^{\circ}00'28.''24260 \pm 0''.00047$  at a reference epoch of 2020.0 with a proper motion of  $\mu_{\alpha^*,sgra} = -3.152 \pm 0.011$  mas yr<sup>-1</sup>,  $\mu_{\delta,sgra} = -5.586 \pm 0.006$  mas yr<sup>-1</sup>.

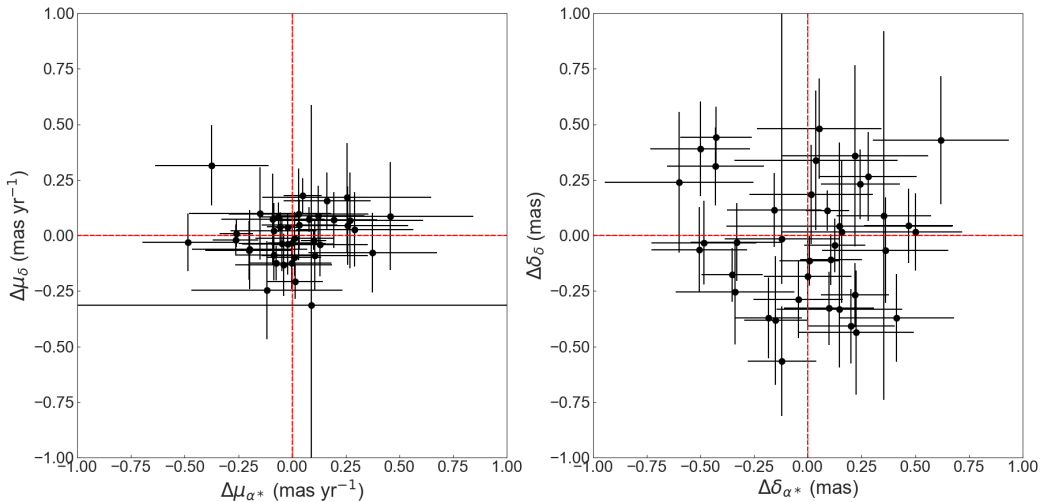


**Figure 5.** The differences between the the HST-Gaia and Gaia-DR3 proper motions (left) and positions (right) for the primary reference stars, which constrain the consistency between the HST-Gaia and Gaia-CRF3 coordinate systems. We find no evidence for systematic biases between the reference frames to a precision of  $0.025 \text{ mas yr}^{-1}$  in proper motion and  $0.044 \text{ mas}$  in position.

the radio sample used to define the most recent maser-based reference frame at the GC (D23). These are used to assess the consistency between the HST-Gaia and radio maser measurements. Note that many of the masers and primary reference stars are located beyond  $R \geq 25''$  from SgrA\* but are included in this sample due to their relevance to the HST-Gaia reference frame. The HST-Gaia measurements in ICRS coordinates are reported in Table 3 along with their corresponding HST photometry in Table 4. In addition, the HST-Gaia measurements transformed into SgrA\*-at-Rest coordinates are provided in Appendix D for convenience.

The stars in this catalog span an HST magnitude range between  $10.95 \text{ mag} < F153M < 20.5 \text{ mag}$ , and the brightest sources ( $F153M \leq 15 \text{ mag}$ ) achieve median position and proper motion errors of  $0.11 \text{ mas}$  and  $0.03 \text{ mas yr}^{-1}$ , respectively (Figure 6). These measurements are  $\sim 20x$  more precise than the ICRS proper motions derived from the VVV survey field that covers the GC region (Griggio et al. 2024). This improvement is enabled by the astrometric performance of the HST WFC3-IR observations and the time baseline of the dataset.

A majority of the stars in the catalog prefer a best-fit kinematic model with multiple kernels. The most commonly preferred model is one that contains a time-based correlation kernel: 47.6% of the sample prefers a *poly+sqexp* model and a further 17.2% prefer a *poly+step* model. Only a small number of stars prefer the *poly+confusion* (2.6%) or *poly+add* models (1.4%). The remaining 31.2% of the sample is best described

using a *poly-only* model, indicating that their astrometry can be described by linear proper motion alone. The fraction of stars that prefer a *poly-only* model is higher for brighter stars ( $\sim 54\%$  of stars with  $F153M < 16 \text{ mag}$ ) compared to fainter stars ( $\sim 28\%$  of stars with  $F153M > 16 \text{ mag}$ ). This distribution suggests that the systematic errors in the HST astrometry are dominated by the PA-dependent shifts discussed in Appendix A, which manifest as a correlation in time and is stronger for fainter stars than for brighter ones.

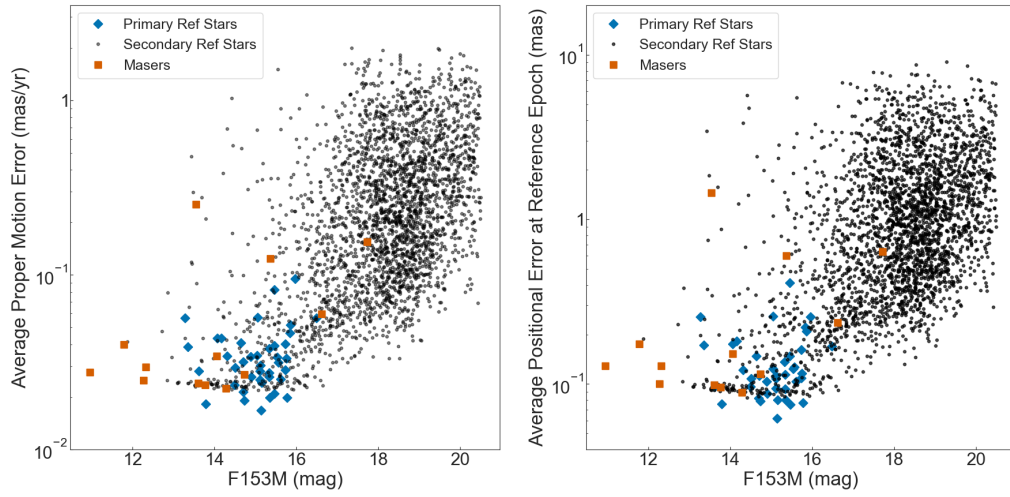


**Figure 6.** Average HST-Gaia proper motion errors (left) and reference epoch position errors (right) as a function of F153M magnitude for the sample of stars presented in this paper. Primary reference stars (from Gaia-DR3) are shown as blue diamonds, newly-created secondary reference stars within  $R \lesssim 1\text{pc}$  from SgrA\* as black points, and the masers used for comparison with radio measurements as red squares. The data points represent the average of the  $\alpha^*$  and  $\delta$  errors for each star.

Table 3. HST-Gaia Proper Motions: ICRS Coordinates

Name	$\alpha$ (deg)	$\delta$ (deg)	$\sigma_{\alpha^*}$ (mas)	$\sigma_{\delta}$ (mas)	$\mu_{\alpha^*}$ (mas/yr)	$\sigma_{\mu_{\alpha^*}}$ (mas/yr)	$\mu_{\delta}$ (mas/yr)	$\sigma_{\mu_{\delta}}$ (mas/yr)	$t_0$ (year)	$\overline{\chi^2_{\text{LOO}}(\alpha^*)}$	$\overline{\chi^2_{\text{LOO}}(\delta)}$	$N$	Model	Ref	Alt Name
HST_NSC_007314	266.41680951	-29.00792399	3.76	3.84	-8.97	0.90	4.47	0.89	2018.4467	1.08	0.99	11	1	0	S0-6
HST_NSC_007079	266.41689152	-29.00800914	1.01	1.00	4.86	0.25	-10.73	0.25	2015.4906	1.75	2.00	9	0	0	S0-9
HST_NSC_006757	266.41697611	-29.00795541	0.43	0.42	0.16	0.18	-6.44	0.18	2019.6907	0.76	0.56	14	0	0	S0-13
HST_NSC_007316	266.41663396	-29.00772225	5.06	1.06	-2.26	0.94	-3.11	0.30	2019.3942	1.16	0.59	12	2	0	S0-12
HST_NSC_007214	266.41657304	-29.00792728	0.40	0.46	-0.20	0.08	-7.48	0.10	2018.5698	0.90	0.96	14	2	0	S0-14
HST_NSC_007322	266.41690889	-29.00759950	1.25	1.25	-11.58	0.38	-2.59	0.38	2012.8189	1.27	1.80	9	0	0	S1-3
HST_NSC_006751	266.41690777	-29.00807787	5.72	5.27	-6.56	0.92	-1.09	0.88	2013.5218	0.43	0.86	11	2	0	S1-5
HST_NSC_016387	266.41654287	-29.00772010	9.01	2.66	4.42	1.83	-7.26	0.66	2017.8891	0.60	1.03	9	5	0	S1-26
HST_NSC_007323	266.41715087	-29.00782874	0.84	0.58	2.01	0.16	-4.64	0.13	2017.6056	0.65	0.90	14	2	0	S1-1
HST_NSC_006701	266.41711206	-29.00767334	0.24	0.22	-12.59	0.05	1.45	0.04	2018.6155	0.60	0.66	13	2	0	irs16C

NOTE—Description of columns: *Name*: HST star name,  $\alpha$ ,  $\delta$ : RA and DEC position at  $t_0$ ,  $\sigma_{\alpha^*}$ ,  $\sigma_{\delta}$ : Uncertainty in  $\alpha^*$  and  $\delta$ , where  $\sigma_{\alpha^*} = \sigma_{\alpha} * \cos(\delta)$ ,  $\mu_{\alpha^*}$ ,  $\mu_{\delta}$ : HST-Gaia proper motions,  $\sigma_{\mu_{\alpha^*}}$ ,  $\sigma_{\mu_{\delta}}$ : error in  $\mu_{\alpha^*}$  and  $\mu_{\delta}$ ,  $t_0$ : reference epoch of the HST-Gaia proper motions (calculated as the astrometric-error weighted average time across the epoch dates in Table 1),  $\overline{\chi^2_{\text{LOO}}(\alpha^*)}$ ,  $\overline{\chi^2_{\text{LOO}}(\delta)}$ : LOO Reduced  $\chi^2$  values for  $\mu_{\alpha^*}$  and  $\mu_{\delta}$  fits, respectively (Eqn 8),  $N$ : Number of F153M epochs observed, *Model*: Specifies the kinematic model used 0: *poly-only*, 1: *poly+conf*, 2: *poly+add*, 3: *poly+scrp*, 4: *poly+scrp*, 5: *poly+scrp*, *Ref*: Type of reference star - 0: Secondary reference star, 1: primary reference star, 2: maser, *AltName*: Alternative name for star, if applicable (either from Sakai et al. (2019) or the Gaia-DR3 catalog)

NOTE—The proper motion fit uncertainties reported in this table ( $\sigma_{\alpha^*}$ ,  $\sigma_{\delta}$ ,  $\sigma_{\mu_{\alpha^*}}$ ,  $\sigma_{\mu_{\delta}}$ ) do not include the systematic error between the HST-Gaia and Gaia-CRF3 discussed in §3.3.

NOTE—The full table is available in machine-readable format.

**Table 4.** HST Photometry

Name	F127M	$\sigma_{F127M}$	F139M	$\sigma_{F139M}$	F153M	$\sigma_{F153M}$	Ref Type	Alt Name
HST_NSC_007314	18.73	0.03	17.40	0.06	16.07	0.05	0	S0-6
HST_NSC_007079	19.10	0.03	17.87	0.06	16.70	0.19	0	S0-9
HST_NSC_006757	18.38	0.02	17.07	0.02	15.70	0.13	0	S0-13
HST_NSC_007316	20.99	0.15	19.17	0.09	17.68	0.09	0	S0-12
HST_NSC_007214	18.85	0.04	17.64	0.03	16.42	0.08	0	S0-14
HST_NSC_007322	-999.00	-999.00	-999.00	-999.00	14.20	0.05	0	S1-3
HST_NSC_006751	18.78	0.02	17.31	0.03	15.62	0.12	0	S1-5
HST_NSC_016387	20.94	0.30	19.54	0.22	17.87	0.15	0	S1-26
HST_NSC_007323	18.01	0.02	16.77	0.02	15.59	0.02	0	S1-1
HST_NSC_006701	15.20	0.01	13.93	0.01	12.72	0.13	0	irs16C

NOTE—Description of columns: *Name*: star name, *F127M*, *F139M*, *F153M*: Vega mags in corresponding filters (F153M is the average mag across all F153M epochs),  $\sigma_{F127M}$ ,  $\sigma_{F139M}$ ,  $\sigma_{F153M}$ : error in corresponding mags ( $\sigma_{F153M}$  is the average error across all F153M epochs), *Ref Code*: Type of ref star – 0: Secondary reference star, 1: primary reference star, 2: maser, *Alt Name*: Alternative name for star, if applicable (e.g. from Sakai et al. 2019, or Gaia-DR3 catalog)

NOTE—Values of -999.0 indicate that the star wasn't detected in that filter. The full table is available in machine-readable format.

#### 4.1.1. Identifying the HST-Gaia Astrometric Reference Stars

The selection of the 40 primary reference stars is described in detail in §3.1. Here we discuss the identification of the secondary reference stars and masers.

The secondary reference stars comprise of well-measured HST-Gaia sources that are located within the 22" x 22" mosaic of ground-based AO observations described by Sakai et al. (2019), which has been observed annually since 2005 as part of the Galactic Center Orbits Initiative (PI: A.M. Ghez; see also Ghez et al. 2008; Yelda et al. 2010; Jia et al. 2019). To remove sources with poor HST-Gaia astrometry, we require that the secondary reference stars meet the following criteria: (1) they must be detected in at least 4 HST epochs and have kinematic motion fits with  $\widetilde{\chi^2_{100}} \leq 5$  (Equation 8); (2) have reference epoch position uncertainties < 10 mas and proper motion uncertainties < 2 mas yr<sup>-1</sup>; (3) have reference epoch position and proper motion uncertainties > 0.01 mas and > 0.01 mas yr<sup>-1</sup>, respectively, removing a small fraction of stars where the kinematic model fit fails and returns unphysically small errors (~1% of total sample); (3) have a total proper motion < 15 mas/yr, to eliminate erroneous high-proper motion sources caused by stellar mismatches or confusion; and (4) have F153M ≤ 20.5 mag. Of an initial set of 3250 HST-Gaia sources within the Sakai et al. (2019) field, 2823 fulfill these criteria and define the secondary reference star sample.

The final set of stars in this catalog are the NIR counterparts to the stellar masers used to define the most recent radio-based astrometric reference frame at the GC from D23. To be matched with a maser source, the HST-Gaia position must match within 0.1" at a common epoch of 2015.5. Of the 15 masers in the D23 sample, 13 are successfully matched with HST-Gaia sources.

#### 4.2. The Consistency Between the HST-Gaia and Radio Maser Reference Frames at the GC

The consistency between the the HST-Gaia reference frame and the most recent radio-based maser reference frame at the GC (D23) is evaluated by comparing the positions and proper motions of the stellar masers present in both catalogs. However, the radio measurements of the masers are made in a SgrA\*-at-Rest coordinate system, and so the HST-Gaia measurements must be transformed into the same system as discussed in §3.4. Thus, the additional uncertainties between the Gaia-CRF3 and ICRS coordinate system (§4.2.1) and the SgrA\* ICRS measurements themselves (§4.2.2) must be taken into account. These uncertainties are summarized in Table 5 and the final comparison between the

HST-Gaia and D23 radio measurements is presented in §4.2.3.

#### 4.2.1. Systematic Uncertainties Between HST-Gaia and ICRS

Since the orientation of Gaia-CRF3 is fixed to ICRS, the HST-Gaia reference frame is also consistent with ICRS. To determine the systematic uncertainty between HST-Gaia and ICRS, the systematic uncertainty between Gaia-CRF3 and ICRS must be considered.

Gaia-CRF3 is aligned to the ICRS using quasar sources in the Gaia-DR3 catalog, with ~0.4 million sources used to fix the rotational state of the reference frame (i.e., asserting that the proper motions of these extragalactic sources are consistent with zero) and ~2000 sources with counterparts in the third realization of the International Celestial Reference Frame (ICRF3; Charlot et al. 2020) to constrain the orientation (Gaia Collaboration et al. 2022a). Maps of the proper motions of over 1 million quasar sources in Gaia-DR3 reveal systematic errors of 0.0112 mas yr<sup>-1</sup> in  $\mu_{\alpha^*}$  and 0.0107 mas yr<sup>-1</sup> in  $\mu_{\delta}$  (Lindegren et al. 2021; Gaia Collaboration et al. 2022a), which we adopt as the systematic proper motion uncertainty between Gaia-CRF3 and ICRS. The uncertainty between the Gaia-CRF3 and ICRS positions is estimated from the position differences of common quasar sources between Gaia-DR3 and ICRF3. Gaia Collaboration et al. (2022a) find the median position difference ( $\alpha^*$  and  $\delta$  combined) to be 0.516 mas across the 3142 such sources. This suggests an error-on-the-mean difference (analogous to Equation 11) of 0.516 mas /  $\sqrt{3142} = 0.009$  mas. Assuming this is evenly split between  $\alpha^*$  and  $\delta$  implies a systematic position uncertainty of 0.007 mas in each direction<sup>4</sup>.

The total systematic uncertainty between HST-Gaia and ICRS is calculated as the quadratic sum of the systematic uncertainty between HST and Gaia-CRF3 (§3.1) and the systematic uncertainty between Gaia-CRF3 and ICRS. The total systematic uncertainty in proper motion is thus  $(\sigma_{\Delta\mu_{\alpha^*}}, \sigma_{\Delta\mu_{\delta}}, \sigma_{\Delta pm}) = (0.023, 0.018, 0.029)$  mas/yr, where  $\sigma_{\Delta pm} = \sqrt{\sigma_{\Delta\mu_{\alpha^*}}^2 + \sigma_{\Delta\mu_{\delta}}^2}$ . The total systematic uncertainty in position is  $(\sigma_{\Delta\alpha^*}, \sigma_{\Delta\delta}, \sigma_{\Delta pos}) = (0.033, 0.031, 0.045)$  mas, where  $\sigma_{\Delta pos} = \sqrt{\sigma_{\Delta\alpha^*}^2 + \sigma_{\Delta\delta}^2}$ . These uncertainties are overwhelmingly dominated by the uncertainty between HST and Gaia-

<sup>4</sup> Gaia Collaboration et al. (2022a) find the median position offsets across the quasar sample (analogous to Eqn 10) to be -0.004 mas and 0.006 mas in  $\alpha^*$  and  $\delta$ , respectively, which is consistent with zero to within the estimated uncertainty of 0.007 mas in each direction.

CRF3, with the Gaia-CRF3 to ICRS step making only a very small contribution.

#### 4.2.2. *HST-Gaia and SgrA\*-at-Rest*

Transforming HST-Gaia measurements into a SgrA\*-at-Rest frame incurs the additional uncertainty in the ICRS measurements of SgrA\* (Xu et al. 2022). These uncertainties are  $(\sigma_{\mu_{\alpha^*}}, \sigma_{\mu_{\delta}}) = (0.011, 0.006)$  mas/yr and  $(\sigma_{\alpha^*}, \sigma_{\delta}) = (0.21, 0.47)$  mas. The total uncertainty between HST-Gaia and the SgrA\*-at-Rest frame is then the quadratic sum of the uncertainties between HST-Gaia and Gaia-CRF3, Gaia-CRF3 and ICRS, and the SgrA\* measurements. This yields  $(\sigma_{\Delta\mu_{\alpha^*}}, \sigma_{\Delta\mu_{\delta}}, \sigma_{\Delta pm}) \sim (0.025, 0.019, 0.031)$  mas/yr and  $(\sigma_{\Delta\alpha^*}, \sigma_{\Delta\delta}, \sigma_{\Delta pos}) \sim (0.213, 0.471, 0.517)$  mas. The total proper motion uncertainty is dominated by the uncertainty between the HST-Gaia and Gaia-CRF3 frames while the total position uncertainty is dominated by the ICRS position of SgrA\*.

#### 4.2.3. *Constraining the Bias Between HST-Gaia and Radio Maser Reference Frames*

We compare the positions and proper motions of 13 masers from D23 that are successfully matched in the HST-Gaia sample<sup>5</sup>. The extent to which a bias may be present between the two frames is quantified using Equations 10 and 11. To measure the position bias, the HST-Gaia and D23 proper motions are used to calculate the maser positions at a common epoch of 2017.4891 (the optimal comparison epoch as calculated via Equation 12).

From the maser measurements alone (i.e. ignoring the systematic reference frame uncertainties from Table 5), we find the average proper motion differences to be  $(-0.076 \pm 0.016, -0.042 \pm 0.020)$  mas/yr in  $(\mu_{\alpha^*}^s, \mu_{\delta}^s)$  and  $(-0.536 \pm 0.088, -0.517 \pm 0.119)$  mas in  $(\delta_{\alpha^*}^s, \delta_{\delta}^s)$ . When the systematic reference frame uncertainties are added in quadrature to the measurement uncertainties, the differences between the HST-Gaia and radio maser frames become  $(-0.076 \pm 0.030, -0.042 \pm 0.028)$  mas/yr in  $(\mu_{\alpha^*}^s, \mu_{\delta}^s)$  and  $(-0.536 \pm 0.230, -0.517 \pm 0.486)$  mas in  $(\delta_{\alpha^*}^s, \delta_{\delta}^s)$  (Figure 7). Thus, the joint probability distribution of the differences in the  $(\mu_{\alpha^*}^s, \mu_{\delta}^s)$  proper motions are consistent with zero to within  $0.041 \text{ mas yr}^{-1}$  at 99.7% confidence. Similarly, the joint probability distribution of the differences in the  $(\delta_{\alpha^*}^s, \delta_{\delta}^s)$  positions are consistent with zero to within 0.54 mas at 99.7% confidence.

<sup>5</sup> The 13 masers used to compare the HST-Gaia and D23 radio maser reference frames are IRS7, IRS12N, IRS9, IRS10EE, IRS15NE, IRS28, IRS17, SiO-15, IRS19NW, SiO-14, SiO-11, SiO-16, and SiO-6.

However, a possible tension at may be present in the  $\alpha^*$  direction in both proper motion and position at  $\sim 2.5\sigma$  significance, which can be seen by the apparent leftward shift in the average differences from zero in Figure 7. This tension could indicate the presence of a systematic error in either the HST-Gaia reference frame, radio maser reference frame, the measured ICRS position and proper motion of SgrA\* from Xu et al. (2022), or some combination of the three. Further improvements in the HST-Gaia and radio measurements are required to determine if this tension is evidence for a true offset or not.

## 5. DISCUSSION

### 5.1. *Uncertainties in the HST-Gaia Measurements and Reference Frame: Comparison with Past Work*

The GC reference frame is a key source of uncertainty when studying the motions and orbits of stars near SgrA\* (e.g. Do et al. 2019; The GRAVITY Collaboration et al. 2024). Here we compare two facets of the uncertainty in the HST-Gaia reference frame to previous GC NIR reference frames in the literature: the overall precision of the reference frame (i.e., the uncertainty in the systematic bias relative to the desired coordinate system) and the uncertainties in the individual position and proper motion measurements for the astrometric reference stars. In summary, the HST-Gaia reference frame offers an improved overall uncertainty compared to past GC NIR reference frames constructed using AO observations of stellar masers, thus lowering the error floor that can be achieved (§5.1.1). However, the individual measurements uncertainties of the astrometric reference stars are generally higher in HST-Gaia compared to AO maser-based frames, which can lead to larger transformation errors when transforming astrometry into the reference frame (§5.1.2).

#### 5.1.1. *The Overall Precision of the Reference Frame*

As discussed in §3.3, the overall precision of a reference frame is quantified by the uncertainty in the systematic bias of the reference frame relative to its desired coordinate system. This represents the maximum possible precision that can be achieved for individual measurements in that reference frame. The uncertainty in the systematic bias of the HST-Gaia reference frame (relative to Gaia-CRF3) is  $(\sigma_{\Delta\mu_{\alpha^*}}, \sigma_{\Delta\mu_{\delta}}, \sigma_{\Delta pm}) = (0.020, 0.015, 0.025)$  mas yr<sup>-1</sup> in proper motion and  $(\sigma_{\Delta\alpha^*}, \sigma_{\Delta\delta}, \sigma_{\Delta pos}) = (0.032, 0.030, 0.044)$  mas in position, which compares favorably to previous GC NIR reference frames constructed via ground-based AO observations of stellar masers (Table 5). In terms of the proper motion, HST-Gaia is  $\sim 4x$  more precise than the ref-

**Table 5.** The Systematic Uncertainties Between Reference Frames

Reference Frame	Coordinate System	$\sigma_{\Delta\mu_{\alpha^*}}$ (mas yr <sup>-1</sup> )	$\sigma_{\Delta\mu_{\delta}}$ (mas yr <sup>-1</sup> )	$\sigma_{\Delta pm}$ (mas yr <sup>-1</sup> )	$\sigma_{\Delta\alpha^*}$ (mas)	$\sigma_{\Delta\delta}$ (mas)	$\sigma_{\Delta pos}$ (mas)	Notes
HST-Gaia	Gaia-CRF3	0.02	0.015	0.025	0.032	0.03	0.044	see §3.1
HST-Gaia	ICRS	0.023	0.018	0.029	0.033	0.031	0.045	see §4.2.1
HST-Gaia	SgrA*-at-Rest	0.025	0.019	0.031	0.213	0.471	0.517	see §4.2.2
Plewa et al. (2015)	SgrA*-at-Rest	0.08	0.07	0.11	0.17	0.17	0.24	AO obs of masers
Sakai et al. (2019)	SgrA*-at-Rest	0.018	0.025	0.031	0.458	0.455	0.646	AO obs of masers

NOTE—As discussed in §4.2.1,  $\sigma_{\Delta pm} = \sqrt{\sigma_{\Delta\mu_{\alpha^*}}^2 + \sigma_{\Delta\mu_{\delta}}^2}$  and  $\sigma_{\Delta pos} = \sqrt{\sigma_{\Delta\alpha^*}^2 + \sigma_{\Delta\delta}^2}$ .

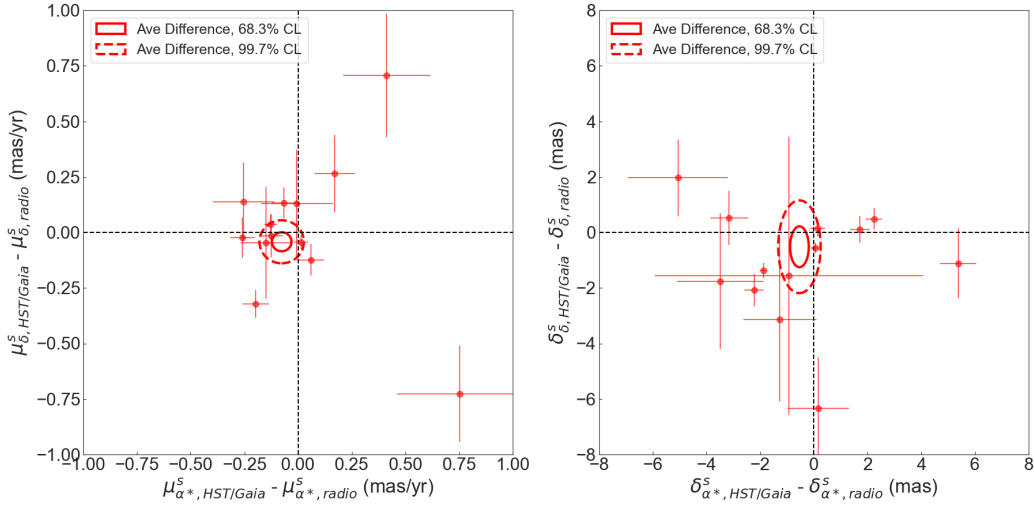


**Figure 7.** Proper motion (left) and position (right) differences for the masers between the HST-Gaia and radio measurements in SgrA\*-at-Rest coordinates (red points). We calculate an average offset of  $(-0.076 \pm 0.030, -0.042 \pm 0.028)$  mas yr<sup>-1</sup> in the  $(\mu_{\alpha^*}^s, \mu_{\delta}^s)$  proper motions and  $(-0.536 \pm 0.231, -0.517 \pm 0.486)$  mas in the  $(\delta_{\alpha^*}^s, \delta_{\delta}^s)$  positions (at a common epoch of 2017.4891). The red circle represents the 68.3% confidence level and the red dashed circle represents the 99.7% confidence level for the average offset. This indicates that the HST-Gaia and radio reference frames are consistent (i.e., the average offset is consistent with zero) to within 99.7% confidence, although with a possible bias in the  $\alpha^*$  directions (in both position and proper motion) at  $\sim 2.5\sigma$  significance.

reference frame from Plewa et al. (2015), which achieves  $(\sigma_{\Delta\mu_{\alpha^*}}, \sigma_{\Delta\mu_{\delta}}, \sigma_{\Delta pm}) = (0.08, 0.07, 0.11)$  mas yr<sup>-1</sup>, and is  $\sim 1.2x$  more precise than the reference frame from Sakai et al. (2019), which achieves  $(\sigma_{\Delta\mu_{\alpha^*}}, \sigma_{\Delta\mu_{\delta}}, \sigma_{\Delta pm}) = (0.018, 0.025, 0.031)$  mas yr<sup>-1</sup>. In terms of the position, the HST-Gaia reference frame is  $\sim 5x$  more precise than Plewa et al. (2015), which achieves  $(\sigma_{\Delta\alpha^*}, \sigma_{\Delta\delta}, \sigma_{\Delta pos}) = (0.17, 0.17, 0.24)$  mas, and is  $\sim 15x$  more precise than Sakai et al. (2019), which achieves  $(\sigma_{\Delta\alpha^*}, \sigma_{\Delta\delta},$

$\sigma_{\Delta pos}) = (0.458, 0.455, 0.646)$  mas<sup>6</sup>. A key advantage of the HST-Gaia reference frame for reducing this error term is the larger number of primary reference stars available to define it (40 Gaia-DR3 sources, compared to only 7 or 8 masers for the AO maser-based frames).

When studying the orbit of the star S0-2/S2, recent studies have incorporated additional constraints into the GC reference frame in order to achieve even higher precision. Such constraints include NIR position measure-

<sup>6</sup> The large position error in Sakai et al. (2019) is primarily due to the Keck NIRC2 distortion correction error of 1 mas added in quadrature to the astrometric errors.

ments of SgrA\* when it is in a bright state (e.g. GRAVITY Collaboration et al. 2020) as well as constraints on the joint dynamical center of multiple Keplerian orbits measured for stars in the region (GRAVITY Collaboration et al. 2022; The GRAVITY Collaboration et al. 2024). These studies report reference frame uncertainties of  $\sigma_{\Delta pm} \lesssim 0.01 \text{ mas yr}^{-1}$  and  $\sigma_{\Delta pos} \lesssim 0.01 \text{ mas}$ . However, in many cases the position and/or proper motion of SgrA\* inferred by the stellar orbits are not consistent with zero within these errors as would be expected for the coordinate system. A similar approach of combining the HST-Gaia reference frame with these additional constraints is beyond the scope of this paper.

### 5.1.2. Position and Proper Motion Uncertainties of Astrometric Reference Stars in the Central Parsec

The precision to which individual astrometric measurements can be transformed into a given reference frame (i.e., the transformation errors) is related to the position and proper motion uncertainties of the astrometric reference stars. The lower the uncertainties of the reference stars, then the lower the transformation errors will be. Here we compare the uncertainties of the HST-Gaia secondary reference stars to the uncertainties of the secondary astrometric standards of the AO maser-based reference frame at the GC from Sakai et al. (2019).

A total of 542 stars are found in common between the HST-Gaia catalog and Sakai et al. (2019) reference star catalogs. The AO measurements are more precise for most sources, with  $\sim 68\%$  of reference stars having more precise AO positions and  $\sim 62\%$  of reference stars having more precise AO proper motions when compared to the corresponding HST-Gaia measurements (Figure 8). This is not unexpected given that the AO observations have higher spatial resolution than HST WFC3-IR (FWHM  $\sim 60 \text{ mas}$  vs. FWHM  $\sim 170 \text{ mas}$ ) and are thus less impacted by stellar crowding. However, for bright sources (F153M  $\leq 16 \text{ mag}$ ), the HST-Gaia measurements are more comparable to the AO measurements, with similar median proper motion errors ( $0.05 \text{ mas yr}^{-1}$  and  $0.06 \text{ mas yr}^{-1}$ , respectively) and median position errors ( $0.20 \text{ mas}$  and  $0.22 \text{ mas}$ , respectively). Stellar confusion has less impact on the astrometry of the brighter sources and so the lower-resolution HST-Gaia measurements become more competitive. On the other hand, the impact of stellar confusion on the HST-Gaia measurements becomes apparent for fainter sources (F153M  $> 16 \text{ mag}$ ), where the AO measurements have lower median proper motion errors ( $0.08 \text{ mas yr}^{-1}$  vs.  $0.13 \text{ mas yr}^{-1}$ ) and position errors ( $0.30 \text{ mas}$  vs.  $0.55 \text{ mas}$ ). The HST-Gaia measurement errors also exhibit significantly increased scatter in this regime (Figure 8).

This comparison suggests that astrometry transformed into the HST-Gaia reference frame may suffer from larger transformation errors compared to when an AO maser-based reference frame is used. One path to mitigate this is to restrict the HST-Gaia reference star sample to the lower-error sources when applying to data. The optimal thresholds to adopt will change depending on the requirements of the given science case as well as the trade-off between using more HST-Gaia reference stars with higher individual uncertainties vs. fewer HST-Gaia reference stars with lower individual uncertainties.

### 5.2. Expected Improvement in the HST-Gaia Reference Frame with Gaia-DR4

The Gaia mission is planning to release a DR4 astrometric catalog sometime after mid-2026 which is expected to deliver significantly improved astrometry relative to the DR3 catalog<sup>7</sup>. These improvements will reduce the astrometric uncertainties of the Gaia primary reference stars and thus also the transformation errors of the HST astrometry. Here we quantify the expected improvement in the HST-Gaia astrometry and predict how it will propagate into the HST-Gaia reference frame.

For a given HST epoch, the transformation uncertainty into the Gaia-CRF3 reference frame can be estimated as:

$$\sigma_{trans} = \alpha_{obs} \frac{\overline{\sigma_{pos}}}{\sqrt{N_{ref} - n_{params}}} \quad (19)$$

where  $\overline{\sigma_{pos}}$  is the average total position uncertainty of the primary reference stars in that epoch,  $N_{ref}$  is the number of reference stars,  $n_{params}$  is the number of parameters in the transformation (6 for a second-order polynomial), and  $\alpha_{obs}$  is an empirically-determined constant. For each reference star,  $\sigma_{pos}$  is the quadratic sum of the HST measurement error and the Gaia catalog position error when propagated to the HST epoch. Using the current values from the transformations described in §3.1, we find that  $\alpha_{obs} \approx 2.4$ .

Gaia DR4 is expected to reduce the Gaia reference epoch position and proper motion uncertainties of the primary reference stars by an average factor of  $\sim 1.6x$  and  $\sim 2.2x$ , respectively. Assuming that no new reference stars are added<sup>8</sup> and recalculating  $\overline{\sigma_{pos}}$  using these

<sup>7</sup> The Gaia mission release schedule can be found at <https://www.cosmos.esa.int/web/gaia/release> and the predictions for the astrometric performance of Gaia DR4 can be found at <https://www.cosmos.esa.int/web/gaia/release>.

<sup>8</sup> This is a conservative assumption, as it is likely that the Gaia DR4 catalog will provide additional primary reference stars in the HST field.

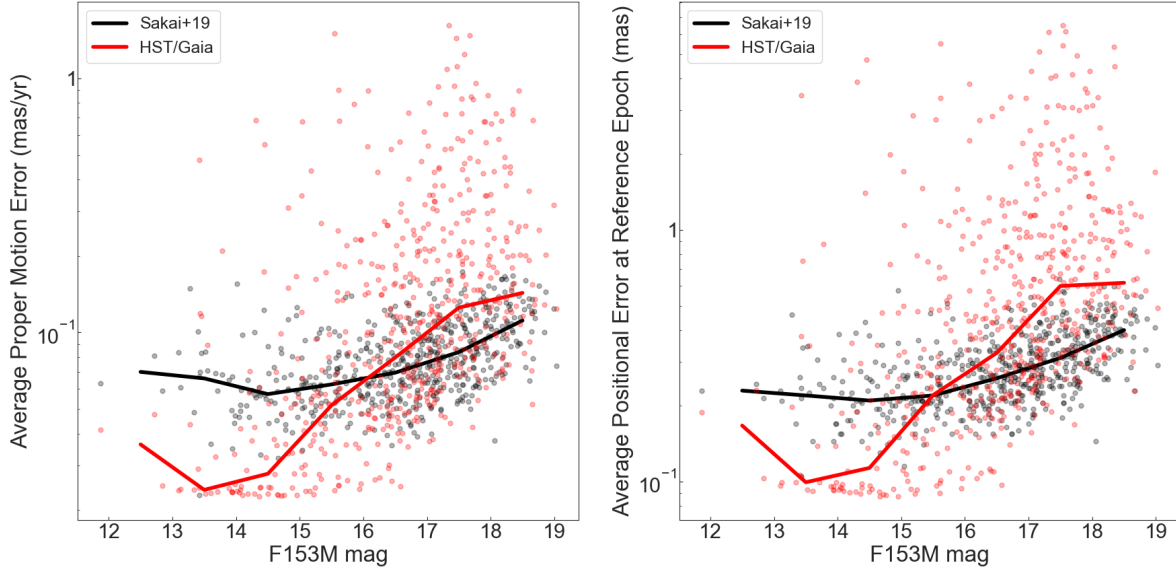


**Figure 8.** The average proper motions errors (left) and reference epoch position errors (right) as a function of F153M magnitude for the 542 stars in common between the HST-Gaia and Sakai et al. (2019) reference star catalogs. The HST-Gaia measurements are shown by the red points and the AO measurements by the black points, with the corresponding lines representing the median errors as a function of magnitude. The precision of the HST-Gaia measurements are comparable to the AO measurements for bright sources ( $F153M \leq 16$  mag) while the AO measurements are more precise for fainter sources ( $F153M > 16$  mag).

improved Gaia uncertainties (while keeping the HST uncertainties the same), we predict that  $\sigma_{trans}$  will range between 0.14 mas and 0.30 mas across the HST epochs. This represents an average of  $\sim 1.7x$  improvement over the current values (e.g., Figure 2).

The constraints on the systematic bias between the HST-Gaia and Gaia-CRF3 reference frame is related to the proper motion precision of the primary reference stars in both the HST-Gaia and Gaia catalog measurements (Equation 11). For the HST-Gaia measurements, the proper motion uncertainty of a given star goes as approximately  $\sigma_{pm} \propto \overline{\sigma_{ast}}$ , where  $\overline{\sigma_{ast}}$  is the average astrometric error across the epochs. The expected improvement in  $\sigma_{trans}$  due to Gaia DR4 results in an improvement of  $\sim 1.4x$  in  $\sigma_{ast}$  and thus the proper motion uncertainties are expected to improve by the same factor. Incorporating this improvement to the HST-Gaia measurements and combining it with the improved Gaia DR4 measurements results in a predicted uncertainty of  $(\sigma_{\Delta\mu_{\alpha^*}}, \sigma_{\Delta\mu_{\delta}}, \sigma_{\Delta pm}) \approx (0.009, 0.009, 0.012)$  mas yr<sup>-1</sup> in the systematic bias between the HST-Gaia and Gaia-CRF3 reference frames. Overall, this represents a factor of  $\sim 2x$  improvement relative to current values.

### 5.3. Applications of the HST-Gaia Reference Frame To GC Science

The precision of the HST-Gaia reference frame enables its application to a wide range of science cases at the GC. The uncertainty in the proper motion bias, which represents the best possible proper motion precision that can be obtained using the HST-Gaia reference frame, has improved over time with the increasing number of HST epochs in the dataset and with successive Gaia catalog releases (Figure 9). Today, the proper motion uncertainty achieved by the HST-Gaia reference frame is within the requirements for science cases such as studying the dynamical structure of the NSC and for probing the extended mass distribution around SgrA\*.

The proximity of the NSC provides a unique opportunity to study the formation and evolution of stars within a galactic nucleus in high detail. Dynamical studies the NSC allows us to constrain its fundamental properties such as its mass, shape, and rotation (e.g. Schödel et al. 2009; Feldmeier et al. 2014; Chatzopoulos et al. 2015), constrain possible formation mechanisms (e.g. Antonini et al. 2012; Do et al. 2020; Arca Sedda et al. 2020; Neumayer et al. 2020), and probe the relationship between the NSC and other stellar structures at the GC (e.g. Nogueras-Lara 2022; Nogueras-Lara et al. 2023). To probe the dynamical structure of the NSC, it is necessary to measure stellar proper motions at a precision that is significantly lower than the velocity dispersion of the cluster ( $\sim 2.1$  mas yr<sup>-1</sup> at the half-light radius; Chat-

zopoulos et al. 2015). To measure such a dispersion at  $3\sigma$  significance would thus require a proper motion precision of  $\sim 0.7 \text{ mas yr}^{-1}$ , which is easily achieved by the HST-Gaia reference frame.

The population of stars and compact remnants at the GC results in a distribution of extended mass around SgrA\* that yields insight into the many dynamical processes near a SMBH. Processes such as dynamical relaxation, mass segregation, stellar collisions, SNe kicks, and tidal disruptions modify the predicted extended mass distribution (e.g. Bahcall & Wolf 1977; Alexander & Hopman 2009; Alexander 2017; Baumgardt et al. 2018; Lini & Sari 2022; Rose & MacLeod 2024; Zhang & Amaro Seoane 2024; Jurado et al. 2024). One approach to explore the extended mass is to measure the additional acceleration it induces on the orbits of stars near the SMBH. This requires a reference frame with a proper motion precision of approximately:

$$\sigma_{pm} \lesssim \frac{GM_{enc}}{r_{apo}} \frac{1}{t_{baseline}} \quad (20)$$

where  $M_{enc}$  is the total enclosed mass within the apocenter of the stellar orbit  $r_{apo}$ ,  $t_{baseline}$  is the time baseline of the reference frame observations, and  $G$  is the gravitational constant. The current HST-Gaia reference frame delivers a minimum proper motion precision that would allow for the detection of an extended mass of  $\sim 3000 M_{\odot}$  within the orbit of the star S0-2 ( $r_{apo} = 0.01 \text{ pc}$ ), and the future improvement from Gaia-DR4 is expected to extend that limit to  $\sim 1000 M_{\odot}$  (Figure 9). Thus, the HST-Gaia reference frame can be used to probe the range  $M_{enc}$  values within S0-2 that are consistent with current observational constraints ( $1200 M_{\odot} - 5500 M_{\odot}$  at the  $1\sigma$  confidence level; Do et al. 2019; GRAVITY Collaboration et al. 2022; The GRAVITY Collaboration et al. 2024). Notably, HST-Gaia is the first ICRS-based reference frame to deliver the precision required for this kind of analysis.

## 6. CONCLUSIONS

We combine multi-epoch HST observations of the GC with the Gaia-DR3 catalog to construct the first high-precision ICRS-based proper motion catalog of NIR astrometric reference sources in the central parsec of the Galaxy. New astrometric measurements are extracted from 14 epochs of HST WFC3-IR astrometry (2010 – 2023) and transformed into the Gaia-CRF3 reference frame using stars in common with Gaia-DR3. Proper motions are measured using a new method that simultaneously models systematic errors in the astrometry via Gaussian Processes. This approach significantly improves the HST proper motion measurements in light

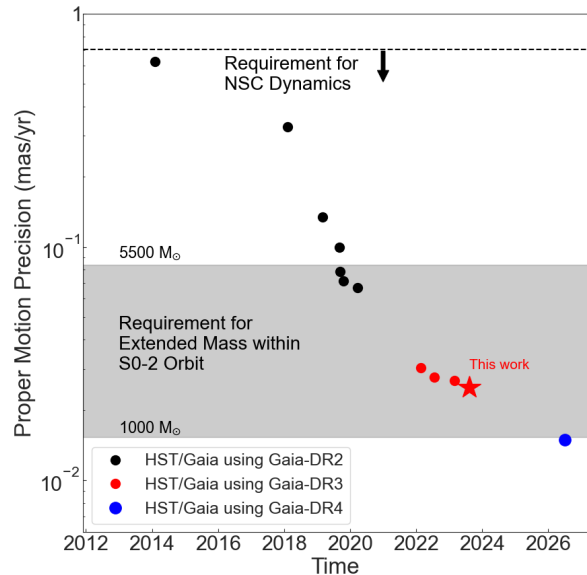


**Figure 9.** The improvement in the proper motion precision of the HST-Gaia reference frame as a function of time, compared to the requirements for various science cases at the GC. The black points correspond to the reference frame precision during the era of Gaia-DR2, the red points during the era of Gaia-DR3 (with the current value represented by the red star), and the blue point is the predicted value that will be achieved once Gaia-DR4 is released (expected sometime after 2026).

of a previously unknown systematic error discovered in the HST WFC3-IR astrometry. We present a catalog of 2876 sources derived from this dataset:

- 40 Gaia-DR3 stars, the primary reference stars used to transform the HST astrometry into the Gaia-CRF3 coordinate system;
- 2823 secondary reference stars within  $R \lesssim 25''$  (1 pc) from SgrA\*, which overlap the region covered by long-term ground-based AO observations monitoring stellar orbits around the SMBH; and
- 13 SiO masers, which are used to evaluate the consistency between HST-Gaia and radio proper motion measurements near the GC.

This catalog defines a novel HST-Gaia astrometric reference frame that can be applied to dynamical studies of stars near the central SMBH.

The HST-Gaia reference frame represents an extension of the ICRS coordinate system (via Gaia-CRF3) into a region of the GC that is inaccessible through Gaia alone. The HST-Gaia astrometric reference stars

have measurement uncertainties as low as  $\sim 0.03$  mas  $\text{yr}^{-1}$  in proper motion and  $\sim 0.11$  mas in reference epoch position, achieving a factor of  $\sim 20$ x improvement over previous ICRS proper motions published in the region (Griggio et al. 2024). The uncertainty in the systematic bias between the HST-Gaia and Gaia-CRF3 reference frames, which represents the best possible precision for HST-Gaia measurements, is  $\sigma_{pm} = 0.025$  mas  $\text{yr}^{-1}$  in proper motion and  $\sigma_{pos} = 0.044$  mas in position. This represents a factor of  $\gtrsim 1.2$ x improvement in proper motion and a factor of  $\gtrsim 4$ x improvement in position relative to previous maser-based GC astrometric reference frames in the NIR (Plewa et al. 2015; Sakai et al. 2019). A key factor driving this improvement is the increased number of primary reference stars available HST-Gaia (40 Gaia-DR3 sources) compared to previous GC NIR reference frames (7 – 8 stellar SiO masers).

In addition, HST-Gaia is the first GC NIR reference frame that is independent of radio measurements of stellar SiO masers near SgrA\*. This enables tests for systematics between the HST-Gaia and radio measurements. We compare the positions and proper motions for 13 stellar masers found in both the HST-Gaia catalog and the most recent radio maser reference frame catalog from D23. After transforming the HST-Gaia measurements into a SgrA\*-at-Rest coordinate system (and accounting for the additional uncertainties incurred), we find that the average difference between the HST-Gaia and radio measurements are  $(-0.076 \pm 0.030, -0.042 \pm 0.028)$  mas  $\text{yr}^{-1}$  in the  $(\mu_{\alpha^*}^s, \mu_{\delta}^s)$  proper motions and  $(-0.536 \pm 0.231, -0.517 \pm 0.486)$  mas in the  $(\delta_{\alpha^*}^s, \delta_{\delta}^s)$  positions. This indicates that the HST-Gaia and radio reference frames are consistent to within 0.041 mas  $\text{yr}^{-1}$  in proper motion and 0.54 mas in position at 99.7% confidence. There is a possible tension in the  $\alpha^*$  direction at  $\sim 2.5\sigma$  significance, but further observations are required to determine if it is indeed real and what its source(s) might be.

Moving forward, the HST-Gaia reference frame can be applied to a range of dynamical science cases at the GC, such as measuring the internal kinematics of the NSC and constraining the enclosed mass within the orbits of stars near SgrA\*. Future improvements will be achieved with the release of the Gaia-DR4 catalog (scheduled for sometime after mid-2026), which we predict will further reduce the overall uncertainty in the HST-Gaia reference frame by an additional factor of  $\sim 2$ x. The complete proper motion catalog of stars derived from the HST-Gaia observations will be published in a future paper (Hosek et al., in prep). This rich dataset will establish a lasting legacy on the dynamical studies of stars near the GC.

## ACKNOWLEDGMENTS

The authors thank the anonymous referee for their feedback which improved the paper. M.W.H. is supported by the Brinson Prize Fellowship, and the authors acknowledge support from the Gordon E. & Betty I. Moore Foundation award #11458. This work is based on observations made with the NASA/ESA Hubble Space Telescope, obtained at the Space Telescope Science Institute, which is operated by the Association of Universities for Research in Astronomy, Inc., under NASA contract NAS 5-26555. The observations are associated with programs GO-11671, GO-12318, GO-12667, GO-13049, GO-15199, GO-15498, GO-16004, GO-15894, GO-16681, and GO-16990. This research has made extensive use of the NASA Astrophysical Data System.

*Facilities:* HST (WFC3-IR), Gaia

*Software:* AstroPy (Astropy Collaboration et al. 2013), texttting2xym\_wfc3ir (a precursor to `hst1pass` described in Anderson 2022), KS2 (Anderson et al. 2008), Matplotlib (Hunter 2007), numPy (Oliphant 2006), SciPy (Virtanen et al. 2020)

## REFERENCES

- Alexander, T. 2017, *ARA&A*, 55, 17
- Alexander, T., & Hopman, C. 2009, *ApJ*, 697, 1861
- Anderson, J. 2022, *One-Pass HST Photometry with hst1pass*, Instrument Science Report WFC3 2022-5, 55 pages, ,
- Anderson, J., et al. 2008, *AJ*, 135, 2055
- Antonini, F., Capuzzo-Dolcetta, R., Mastrobuono-Battisti, A., & Merritt, D. 2012, *ApJ*, 750, 111
- Arca Sedda, M., Gualandris, A., Do, T., et al. 2020, *ApJL*, 901, L29
- Arenou, F., et al. 2018, *A&A*, 616, A17
- Arias, E. F., Charlot, P., Feissel, M., & Lestrade, J. F. 1995, *A&A*, 303, 604
- Astropy Collaboration, Robitaille, et al. 2013, *A&A*, 558, A33
- Bahcall, J. N., & Wolf, R. A. 1977, *ApJ*, 216, 883
- Baumgardt, H., Amaro-Seoane, P., & Schödel, R. 2018, *A&A*, 609, A28
- Bellini, A., Anderson, J., Bedin, L. R., et al. 2017, *ApJ*, 842, 6
- Bellini, A., et al. 2018, *ApJ*, 853, 86
- Charlot, P., et al. 2020, *A&A*, 644, A159
- Chatzopoulos, S., Fritz, T. K., Gerhard, O., et al. 2015, *MNRAS*, 447, 948
- Darling, J., Paine, J., Reid, M. J., et al. 2023, *ApJ*, 955, 117
- Do, T., David Martinez, G., Kerzendorf, W., et al. 2020, *ApJL*, 901, L28
- Do, T., et al. 2019, *Science*, 365, 664
- Dodds-Eden, K., et al. 2011, *ApJ*, 728, 37
- Fabricius, C., et al. 2021, *A&A*, 649, A5
- Feldmeier, A., et al. 2014, *A&A*, 570, A2
- Gaia Collaboration, Klioner, et al. 2022a, *A&A*, 667, A148
- Gaia Collaboration, Vallenari, et al. 2022b, *arXiv e-prints*, [arXiv:2208.00211](https://arxiv.org/abs/2208.00211)
- Gelman, A., Hwang, J., & Vehtari, A. 2013, *Understanding predictive information criteria for Bayesian models*, , [arXiv:1307.5928](https://arxiv.org/abs/1307.5928). <https://arxiv.org/abs/1307.5928>
- Ghez, A. M., et al. 2003, *ApJL*, 586, L127
- Ghez, A. M., et al. 2008, *ApJ*, 689, 1044
- Gillessen, S., Eisenhauer, F., Trippe, S., et al. 2009, *ApJ*, 692, 1075
- Gonidakis, I., Diamond, P. J., & Kemball, A. J. 2010, *MNRAS*, 406, 395
- Gordon, D., de Witt, A., & Jacobs, C. S. 2023, *AJ*, 165, 49
- GRAVITY Collaboration, Abuter, et al. 2018, *ArXiv e-prints*, [arXiv:1807.09409](https://arxiv.org/abs/1807.09409)
- . 2020, *arXiv e-prints*, [arXiv:2004.07187](https://arxiv.org/abs/2004.07187)
- GRAVITY Collaboration, Abuter, et al. 2022, *A&A*, 657, L12
- Griggio, M., Libralato, M., Bellini, A., et al. 2024, *arXiv e-prints*, [arXiv:2403.12219](https://arxiv.org/abs/2403.12219)
- Hornstein, S. D., Ghez, A. M., Tanner, A., et al. 2002, *ApJL*, 577, L9
- Hosek, M. W., Do, T., Lu, J. R., et al. 2022, *ApJ*, 939, 68
- Hosek, Jr., M. W., Lu, J. R., Anderson, J., et al. 2015, *ApJ*, 813, 27
- . 2018, *ApJ*, 855, 13
- Hunter, J. D. 2007, *Computing in Science & Engineering*, 9, 90
- Jia, S., et al. 2019, *ApJ*, 873, 9
- Jia, S., et al. 2023, *arXiv e-prints*, [arXiv:2302.02040](https://arxiv.org/abs/2302.02040)
- Jurado, C., Naoz, S., Lam, C. Y., & Hoang, B.-M. 2024, *ApJ*, 971, 95
- Kemball, A. J. 2007, in *Astrophysical Masers and their Environments*, ed. J. M. Chapman & W. A. Baan, Vol. 242, 236–245
- Lindgren, L., et al. 2021, *A&A*, 649, A2
- Linial, I., & Sari, R. 2022, *ApJ*, 940, 101
- Lu, J. R., Ghez, A. M., Hornstein, S. D., et al. 2009, *ApJ*, 690, 1463
- Menten, K. M., Reid, M. J., Eckart, A., & Genzel, R. 1997, *ApJL*, 475, L111
- Neumayer, N., Seth, A., & Böker, T. 2020, *A&A Rv*, 28, 4
- Nogueras-Lara, F. 2022, *arXiv e-prints*, [arXiv:2208.13218](https://arxiv.org/abs/2208.13218)
- Nogueras-Lara, F., Schultheis, M., Najarro, F., et al. 2023, *A&A*, 671, L10
- Oliphant, T. E. 2006, *A guide to NumPy*, Vol. 1 (Trelgol Publishing USA)
- Paugnat, H., et al. 2024, *ApJ*, 977, 228
- Paumard, T., et al. 2006, *ApJ*, 643, 1011
- Plewa, P. M., et al. 2015, *MNRAS*, 453, 3234
- Rasmussen, C. E., & Williams, C. K. I. 2006, *Gaussian Processes for Machine Learning*
- Reid, M. J., & Brunthaler, A. 2004, *ApJ*, 616, 872
- . 2020, *ApJ*, 892, 39
- Reid, M. J., Menten, K. M., Genzel, R., et al. 2003, *ApJ*, 587, 208
- Reid, M. J., Menten, K. M., Trippe, S., Ott, T., & Genzel, R. 2007, *ApJ*, 659, 378
- Rose, S. C., & MacLeod, M. 2024, *ApJL*, 963, L17
- Sakai, S., et al. 2019, *ApJ*, 873, 65
- Schödel, R., Merritt, D., & Eckart, A. 2009, *A&A*, 502, 91
- Schödel, R., Najarro, F., Muzic, K., & Eckart, A. 2010, *A&A*, 511, A18
- Schödel, R., et al. 2002, *Nature*, 419, 694
- The GRAVITY Collaboration, El Dayem, et al. 2024, *arXiv e-prints*, [arXiv:2409.12261](https://arxiv.org/abs/2409.12261)

Vehtari, A., Gelman, A., & Gabry, J. 2015, arXiv e-prints, arXiv:1507.04544

Vehtari, A., Gelman, A., & Gabry, J. 2016, *Statistics and Computing*, 27, 1413–1432.  
<http://dx.doi.org/10.1007/s11222-016-9696-4>

Virtanen, P., et al. 2020, *Nature Methods*, 17, 261

von Fellenberg, S. D., et al. 2022, *ApJL*, 932, L6

Weldon, G. C., et al. 2023, *ApJL*, 954, L33

Xu, S., Zhang, B., Reid, M. J., et al. 2022, arXiv e-prints, arXiv:2210.03390

Yelda, S., Lu, J. R., Ghez, A. M., et al. 2010, *ApJ*, 725, 331

Zhang, F., & Amaro Seoane, P. 2024, *ApJ*, 961, 232

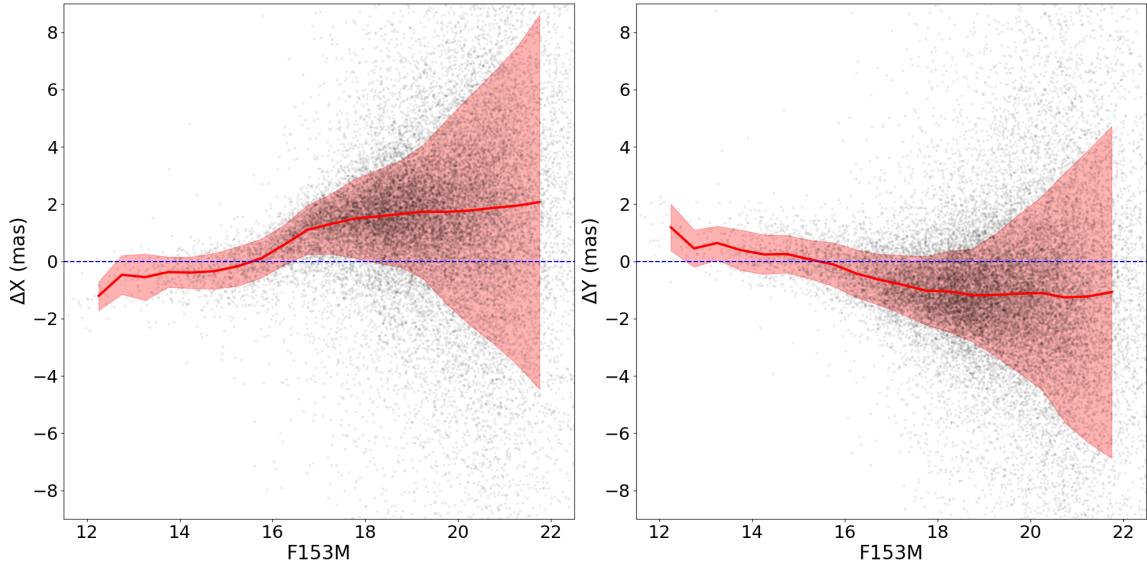


**Figure 10.** Systematic difference in HST astrometry measured at PA =  $-45^\circ$  and PA =  $134^\circ$  epochs as a function of magnitude, in detector X and Y coordinates (left and right panels, respectively). The red line and shaded region shows the average and standard deviation of the position difference, which reaches  $\sim 2$  mas for fainter stars.

## APPENDIX

### A. A SYSTEMATIC ERROR IN HST WFC3-IR ASTROMETRY WITH POSITION ANGLE

Due to restrictions on the HST orbital visibility, the GC observations were taken at two PAs separated by 180 degrees depending on the time of year. A systematic offset in the HST astrometry was found between observations taken at these different PAs. The size of the offset increases as a function of magnitude such that the positions of fainter stars shift by  $\sim 2$  mas in both the X and Y directions on the detector (Figure 10). When rotated onto the plane of the sky, this shift manifests almost entirely the DEC direction.

The offset appears to remain constant over the time baseline of the observations, as linear proper motions derived from only the PA =  $-45^\circ$  epochs (8 epochs between 2010.6261 – 2023.6178) and only the PA =  $134^\circ$  epochs (6 epochs between 2014.099 – 2023.1535) are fully consistent within uncertainties (Figure 11).

The cause of this systematic offset is not yet clear. If it were caused by uncorrected optical distortion, then we would expect the position shift to be a function of location on the detector rather than a function of magnitude, since bright and faint stars would presumably be equally impacted by the distortion. Similarly, if there were a bias in the astrometric reference frame between the different PAs (for example, if induced by parallax in the reference stars), then we would also expect it to impact both bright and faint stars equally.

We hypothesize that this systematic may be explained by a drift in the HST pointing over the length of the individual exposures (349 seconds). All F153M astrometric observations were obtained using the STEP50 up-the-ramp sampling sequence. In this setup, the positions of bright stars come from an average of the first few detector reads before non-linearity/saturation is reached, while the positions of fainter stars come from averaging all the reads across the exposure. Thus, a drift in the telescope pointing during an exposure would result in an apparent position shift between the bright and faint stars (Anderson 2022). If the telescope drift were consistent in both direction and amplitude (relative to detector coordinates) across the dataset, then the position offset would only become apparent when the observation PA is changed, since the direction of the position shift on the sky would change. However, further investigation into this systematic is required to definitively establish its origin.

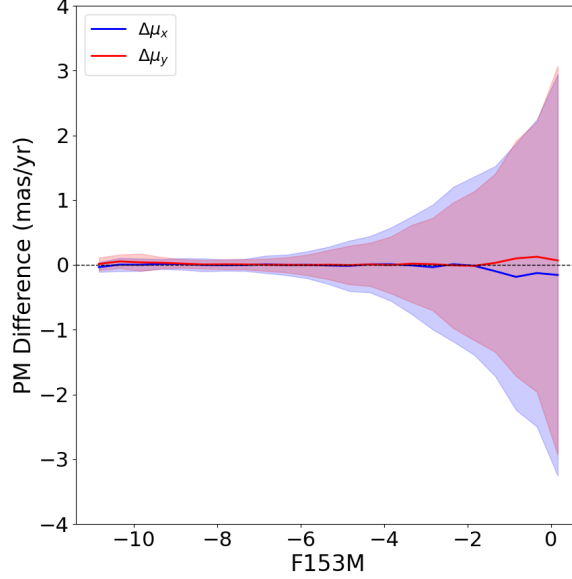


**Figure 11.** The difference between proper motions measured from  $PA = -45^\circ$  and  $PA = 134^\circ$  epochs independently as a function of mag. The red and blue lines and corresponding shaded regions correspond to the average and standard deviation of the differences in the detector X and Y directions, respectively. There are no significant differences in the proper motions, suggesting that the systematic position offset is constant in amplitude and direction (relative to the detector) across the dataset.

## B. MODELING POLYNOMIAL MOTION USING GAUSSIAN PROCESSES

Gaussian processes are a powerful and generic statistical tool that are used to model, parameterically or non-parameterically, a wide-range of physical processes (Rasmussen & Williams 2006). For our purposes, we define a Gaussian Process as a process whose predicted observable is described by a linear model ( $\mathbf{f}(\mathbf{t}) = \mathbf{A}(\mathbf{t})\mathbf{w}$ ), and whose measured observables ( $\mathbf{x}$ ) and parameters ( $\mathbf{w}$ ) (prior probability densities) are normally distributed:

$$\mathbf{x} \mid \mathbf{w} \sim \mathcal{N}(\mathbf{A}(\mathbf{t}) \cdot \mathbf{w}, \Sigma) \quad (\text{B1})$$

$$\mathbf{w} \sim \mathcal{N}(\mathbf{0}, \Sigma_p). \quad (\text{B2})$$

Note that the matrix  $\mathbf{A}(\mathbf{t})$  can be any function of any set of conditional parameters,  $\mathbf{t}$ . Here we impose that  $\mathbf{w}$  is distributed about  $\mathbf{0}$  as to minimize the effect of unconstrained parameters on the resultant posterior distributions. Under these assumptions, the marginal likelihood (marginalized over  $\mathbf{w}$ ) is

$$\mathbf{x} \mid \mathbf{t} \sim \mathcal{N}(\mathbf{0}, \Sigma + \mathbf{K}(\mathbf{t}, \mathbf{t})) \quad (\text{B3})$$

and any predicted observable corresponding to  $\mathbf{t}_p$  ( $\mathbf{f}(\mathbf{t}_p) = \mathbf{A}(\mathbf{t}_p)\mathbf{w}$ ) is normally distributed with a mean and variance of

$$\mathbb{E}_{\mathbf{w}|\mathbf{x},\mathbf{t}}[\mathbf{f}(\mathbf{t}_p)] = \mathbf{K}(\mathbf{t}_p, \mathbf{t}) (\Sigma + \mathbf{K}(\mathbf{t}, \mathbf{t}))^{-1} \mathbf{x} \quad (\text{B4a})$$

$$\mathbb{V}_{\mathbf{w}|\mathbf{x},\mathbf{t}}[\mathbf{f}(\mathbf{t}_p)] = \mathbf{K}(\mathbf{t}_p, \mathbf{t}_p) - \mathbf{K}(\mathbf{t}_p, \mathbf{t}) (\Sigma + \mathbf{K}(\mathbf{t}, \mathbf{t}))^{-1} \mathbf{K}(\mathbf{t}, \mathbf{t}_p) \quad (\text{B4b})$$

where  $\mathbb{E}_{\mathbf{x}|\dots}[\mathbf{f}(\mathbf{x})] \equiv \int \mathbf{f}(\mathbf{x})\mathcal{P}(\mathbf{x} \mid \dots)d\mathbf{x}$  is the expectation,  $\mathbb{V}_{\mathbf{x}|\dots}[\mathbf{f}(\mathbf{x})] \equiv \int (\mathbf{f}(\mathbf{x}))^2 \mathcal{P}(\mathbf{x} \mid \dots)d\mathbf{x}$  is the variance, and  $\mathbf{K}(\mathbf{t}, \mathbf{t}') = \mathbf{A}(\mathbf{t})\Sigma_p\mathbf{A}^\top(\mathbf{t}')$  is defined as the kernel. Or equivalently, the kernel can be expressed as a mean and covariance of  $\mathbf{f}(\mathbf{t})$ :

$$m(\mathbf{t}) = \mathbb{E}_{\mathbf{w}}[\mathbf{f}(\mathbf{t}; \mathbf{w})] \quad (\text{B5})$$

$$K(\mathbf{t}, \mathbf{t}') = \mathbb{E}_{\mathbf{w}}[(\mathbf{f}(\mathbf{t}; \mathbf{w}) - m(\mathbf{t}))(\mathbf{f}(\mathbf{t}'; \mathbf{w}) - m(\mathbf{t}'))] \quad (\text{B6})$$

Note that here, by convention,  $m(\mathbf{t}) = \mathbf{0}$ .

### B.1. polynomial kernels

Since polynomial motion is linear with respect to the polynomial moments, a  $N$ -th order polynomial motion can be described by a Gaussian Process where

$$\begin{aligned} \mathbf{f}(\mathbf{t}) &= x_0 + v(\mathbf{t} - t_0) + \frac{a}{2}(\mathbf{t} - t_0)^2 + \frac{j}{6}(\mathbf{t} - t_0)^3 + \dots \\ &= \mathbf{A}\mathbf{w} \end{aligned} \tag{B7}$$

$$\mathbf{w} \equiv [x_0, v, a, j, \dots]^T \tag{B8}$$

$$\mathbf{t} = [t_1, t_2, \dots]^T \tag{B9}$$

and

$$\mathbf{A} = \begin{bmatrix} 1 & (t_1 - t_0) & \frac{1}{2}(t_1 - t_0)^2 & \frac{1}{6}(t_1 - t_0)^3 & \dots & \frac{1}{N!}(t_1 - t_0)^N \\ 1 & (t_2 - t_0) & \frac{1}{2}(t_2 - t_0)^2 & \frac{1}{6}(t_2 - t_0)^3 & \dots & \frac{1}{N!}(t_2 - t_0)^N \\ \vdots & \vdots & \vdots & \vdots & \vdots & \vdots \end{bmatrix}. \tag{B10}$$

With little loss in generality, we assume  $\Sigma_p$  is diagonal,  $\Sigma_{p,mn} = \sigma_n^2 \delta_{mn}$ . With this, the Kernel element for a polynomial becomes:

$$K^{(\text{poly})}(t, t') = \sum_{n=0}^N \frac{\sigma_n^2}{(n!)^2} [(t - t_0)(t' - t_0)]^n. \tag{B11}$$

Depending on the parameterization of  $\sigma_p$ , the polynomial kernel reduces to:

$$K^{(\text{poly})}(t, t') = \begin{cases} \sigma_0^2 \exp \left[ \left( \frac{t-t_0}{\tau} \right) \left( \frac{t'-t_0}{\tau} \right) \right]; & \sigma_n^2 = n! \left( \frac{\sigma_0}{\tau^n} \right)^2 \\ & N \rightarrow \infty \\ \sigma_0^2 \left[ 1 + \left( \frac{t-t_0}{\tau} \right) \left( \frac{t'-t_0}{\tau} \right) \right]^N; & \sigma_n^2 = \frac{n! N!}{(N-n)!} \left( \frac{\sigma_0}{\tau^n} \right)^2 \end{cases} \tag{B12}$$

Note that the top and bottom parameterizations in Equation B12 correspond to an infinite and finite polynomial, respectively.

### B.2. polynomial moment predictions

In our case, we are interested in constraining the moments of the polynomial. Any order moment of the polynomial can be directly inferred from Equation B4, with the understanding that when calculating higher order moments, derivatives are applied only to the polynomial component,  $f^{(n)}(t) \equiv d^n f(t)/dt^n = d^n f^{(\text{poly})}(t)/dt^n$ . Since any order polynomial moment is a linear model, its prediction is also normally distributed with the mean and covariance of

$$\mathbb{E}_{\mathbf{w}|\mathbf{x}} [f^{(n)}(t')] \equiv \mathbb{E}_{\mathbf{w}|\mathbf{x}} \left[ \frac{d^n}{d\tilde{t}^n} f(\tilde{t}) \Big|_{\tilde{t}=t'} \right] \tag{B13}$$

$$= \frac{d^n}{d\tilde{t}^n} \mathbb{E}_{\mathbf{w}|\mathbf{x}} [f(\tilde{t})] \Big|_{\tilde{t}=t'} \tag{B14}$$

$$= \frac{\partial^n}{\partial \tilde{t}^n} K^{(\text{poly})}(\tilde{t}, \mathbf{t}) \Big|_{\tilde{t}=t'} (\Sigma + \mathbf{K}(\mathbf{t}, \mathbf{t}))^{-1} \mathbf{x} \tag{B15}$$

and

$$\mathbb{C}_{\mathbf{w}|\mathbf{x}} [f^{(m)}(t'), f^{(n)}(t')] \equiv \mathbb{C}_{\mathbf{w}|\mathbf{x}} \left[ \frac{d^m}{d\tilde{t}^m} f(\tilde{t}) \Big|_{\tilde{t}=t'}, \frac{d^n}{d\tilde{t}'^n} f(\tilde{t}') \Big|_{\tilde{t}'=t'} \right] \tag{B16}$$

$$= \frac{d^m}{d\tilde{t}^m} \frac{d^n}{d\tilde{t}'^n} \mathbb{C}_{\mathbf{w}|\mathbf{x}} [f(\tilde{t}), f(\tilde{t}')] \Big|_{\tilde{t}=t', \tilde{t}'=t'} \tag{B17}$$

$$\begin{aligned} &= \frac{\partial^m}{\partial \tilde{t}^m} \frac{\partial^n}{\partial \tilde{t}'^n} K^{(\text{poly})}(\tilde{t}, \tilde{t}') \Big|_{\tilde{t}=t', \tilde{t}'=t'} \\ &\quad - \frac{\partial^m}{\partial \tilde{t}^m} K^{(\text{poly})}(\tilde{t}, \mathbf{t}) \Big|_{\tilde{t}=t'} (\Sigma + \mathbf{K}(\mathbf{t}, \mathbf{t}))^{-1} \frac{\partial^n}{\partial \tilde{t}'^n} K^{(\text{poly})}(\mathbf{t}, \tilde{t}') \Big|_{\tilde{t}'=t'}. \end{aligned} \tag{B18}$$

Here,  $\mathbb{C}_{\mathbf{x}|\dots} [f(\mathbf{x}), g(\mathbf{x})] \equiv \int (f(\mathbf{x}) - \mathbb{E}_{\mathbf{x}|\dots} [f(\mathbf{x})]) (g(\mathbf{x}) - \mathbb{E}_{\mathbf{x}|\dots} [g(\mathbf{x})]) \mathcal{P}(\mathbf{x} | \dots) d\mathbf{x}$  is the covariance.

### B.3. time correlated kernels

Systematics such as those in Appendix A manifest as positional shifts in time. Here, we model this effect as a shift within some window of width  $\tau$  centered at time  $t_0$ . To account for the varying position position shifts these systematics cause at different times, several window functions are used, each weighted independently:

$$f(t; t_0) = \sum_i w_i W(t - t_{0,i}) \quad (\text{B19})$$

For generality,  $\{t_{0,i}\}$ , and its associated weights,  $\{w_i\}$ , can be described as a grid with spacing of  $\Delta t_0$ , where the normal priors of  $\{w_i\}$  centered at *zero* minimizes the effect of any unconstrained  $t_{0,i}$ . If an infinitely large grid of infinitesimal spacing ( $\Delta t_0 \rightarrow 0$ ) is assumed, the Kernel for this process can be reduced to

$$K(t, t') = \sum_i \sigma_i^2 W(t - t_{0,i}) W(t' - t_{0,i}) \quad (\text{B20})$$

$$= \sigma_0^2 \sum_i \frac{\Delta t_0}{Z} W(t - t_{0,i}) W(t' - t_{0,i}) \quad (\text{B21})$$

$$\approx \sigma_0^2 \int \frac{dt_0}{Z} W(t - t_0) W(t' - t_0) \quad (\text{B22})$$

where the covariance of the prior on  $\mathbf{w}$  is assumed to be diagonal with values of  $\sigma_i^2 \equiv \Sigma_{p,ii} = \sigma_0^2 \Delta t_0 / Z$  and  $Z = \int W(t)^2 dt$ . Here, we use two window functions, a step function and a squared exponential window function:

$$W^{(\text{step})}(t) = \begin{cases} 1 & \text{for } |t| \leq \frac{\tau}{2} \\ 0 & \text{for } |t| > \frac{\tau}{2} \end{cases} \quad (\text{B23})$$

$$W^{(\text{sqexp})}(t) = \exp\left[-\frac{t^2}{\tau^2}\right] \quad (\text{B24})$$

These lead to the kernels:

$$K^{(\text{step})}(t, t') = \sigma_0^2 \times \begin{cases} 1 - \left|\frac{t-t'}{\tau}\right| & \text{for } |t-t'| \leq \tau \\ 0 & \text{for } |t-t'| > \tau \end{cases} \quad (\text{B25})$$

and

$$K^{(\text{sqexp})}(t, t') = \sigma_0^2 \exp\left[-\frac{(t-t')^2}{2\tau^2}\right]. \quad (\text{B26})$$

### B.4. spatial correlated kernels

Systematics due to confusion with unresolved point sources can manifest as spatially correlated observations. Again, we model this effect as a shift weighted by some window of width  $\ell$  with the exception that this shift is toward some position  $\mathbf{r}_0 = \{x_0, y_0\}$ . Again by assuming a grid of  $\mathbf{r}_c$ , each with its own weight, leads to a perturbation of

$$f(\mathbf{r}; \mathbf{r}_0) = \sum_i w_i (\mathbf{r} - \mathbf{r}_{0,i}) W(\mathbf{r} - \mathbf{r}_{0,i}). \quad (\text{B27})$$

The kernel as a function of the real spatial coordinates,  $\mathbf{r}$  can be shown to be

$$K(\mathbf{r}, \mathbf{r}') = \sum_i \sigma_i^2 (\mathbf{r} - \mathbf{r}_{0,i})(\mathbf{r}' - \mathbf{r}_{0,i}) W(\mathbf{r} - \mathbf{r}_{0,i}) W(\mathbf{r}' - \mathbf{r}_{0,i}) \quad (\text{B28})$$

$$= \sigma_0^2 \sum_i \frac{\Delta \mathbf{r}_0}{Z} (\mathbf{r} - \mathbf{r}_{0,i})(\mathbf{r}' - \mathbf{r}_{0,i}) W(\mathbf{r} - \mathbf{r}_{0,i}) W(\mathbf{r}' - \mathbf{r}_{0,i}) \quad (\text{B29})$$

$$\approx \sigma_0^2 \int \frac{d\mathbf{r}_0}{Z} (\mathbf{r} - \mathbf{r}_0)(\mathbf{r}' - \mathbf{r}_0) W(\mathbf{r} - \mathbf{r}_0) W(\mathbf{r}' - \mathbf{r}_0) \quad (\text{B30})$$

where the covariance of the prior on  $\mathbf{w}$  is assumed to be diagonal with values of  $\sigma_i^2 \equiv \Sigma_{p,ii} = \sigma_0^2 \Delta \mathbf{r}_0 / Z$  and  $Z = \int \mathbf{r}^2 W(\mathbf{r})^2 d\mathbf{r}$ . For an squared exponential window function of

$$W(\mathbf{r}) = \exp\left[-\frac{|\mathbf{r}|^2}{\ell^2}\right], \quad (\text{B31})$$

the kernel becomes:

$$K(\mathbf{r}, \mathbf{r}') = \sigma_0^2 \left[ \mathbf{1} - \frac{(\mathbf{r} - \mathbf{r}')(\mathbf{r} - \mathbf{r}')}{\ell^2} \right] \exp \left[ -\frac{|\mathbf{r} - \mathbf{r}'|^2}{2\ell^2} \right] \quad (\text{B32})$$

Unfortunately,  $r$ , and thus the dispersion, is dependant on the polynomial motion being modeled, making marginalization of the polynomial parameters non-trivial. Here we make a normal approximation of the marginal probability density by setting resultant variance using Equation B6:

$$K^{(\text{conf})}(t, t') = \mathbb{E}_{w_t, w_r} [\mathbf{r}(t)\mathbf{r}(t')^T] \quad (\text{B33})$$

$$= \mathbb{E}_{w_t} [K(\mathbf{r}(t), \mathbf{r}(t'))]. \quad (\text{B34})$$

Note that here the mean evaluates to zero. This results in a dispersion of:

$$K^{(\text{conf})}(t, t') = \sigma_0^2 \frac{\left[ \mathbf{1} + \frac{K^{(\text{tot})}(t, t) + K^{(\text{tot})}(t', t') - 2\mathbf{K}^{(\text{tot})}(t, t')}{\ell^2} \right]^{-1}}{\sqrt{\left| \mathbf{1} + \frac{K^{(\text{tot})}(t, t) + K^{(\text{tot})}(t', t') - 2\mathbf{K}^{(\text{tot})}(t, t')}{\ell^2} \right|}} \quad (\text{B35})$$

where  $\mathbf{K}^{(\text{tot})}$  is the full covariance matrix in  $x$  and  $y$ .

$$K^{(\text{tot})}(t, t') = \begin{bmatrix} K_x(t, t') & 0 \\ 0 & K_y(t, t') \end{bmatrix}. \quad (\text{B36})$$

and  $K_x(t, t')$  and  $K_y(t, t')$  are the polynomial and time-dependent covariances in the  $x$  and  $y$  directions.

### B.5. hyper-parameters fitting and penalty term

For the above kernels, we fit the hyper-parameters,  $\ell$ ,  $\tau$ , and  $\sigma_0^2$ , by minimizing the marginal likelihood (Equation B3). Since the Gaussian Processes model physical effects as correlations, any unaccounted for temporal auto-correlations in the data can bias the results. This has the largest affect on  $\tau$  and  $t_0$ , usually causing these quantities to sometimes diverge. For this reason, we set  $t_0$  to the weighted average and impose a prior on  $\tau$  of

$$\mathcal{P}(\tau) \propto \frac{1}{1 + \tau}. \quad (\text{B37})$$

### B.6. leave-one-out cross-validation (LOO-CV) and the expected-log-probability-density (ELPD)

Leave-one-out cross-validation (LOO-CV) compares predicted results to a subset of data,  $\mathbf{x}_k$ , when the model is fitted to a data set that excludes this subset,  $\mathbf{x}_{-k} = \{\mathbf{x}_0, \dots, \mathbf{x}_{k-1}, \mathbf{x}_{k+1}, \dots\}$  ( $\mathcal{P}(\mathbf{x}_k | \mathbf{x}_{-k})$ ). If the hyper-parameters are not expected to change a significant amount when one data point is removed, then the variance in the marginalized parameters,  $\mathbf{w}$ , will dominate. Because in a Gaussian process model the predicted values are also normally distributed, one can calculate the predicted value of a single data point ( $x_{\text{loo}_k}$ ) and variance of that point ( $\sigma_{\text{loo}_k}^2$ ):

$$x_{\text{loo}_k} = \mathbf{K}(t_k, \mathbf{t}_{-k}) (\boldsymbol{\Sigma}_{-k} + \mathbf{K}(\mathbf{t}_{-k}, \mathbf{t}_{-k}))^{-1} \mathbf{x}_{-k} \quad (\text{B38})$$

$$\sigma_{\text{loo}_k}^2 = \boldsymbol{\Sigma}_k + \mathbf{K}(t_k, t_k) - \mathbf{K}(t_k, \mathbf{t}_{-k}) (\boldsymbol{\Sigma}_{-k} + \mathbf{K}(\mathbf{t}_{-k}, \mathbf{t}_{-k}))^{-1} \mathbf{K}(\mathbf{t}_{-k}, t_k) \quad (\text{B39})$$

(see Equation B4). Here,  $\boldsymbol{\Sigma}$  is assume to diagonal with elements  $\{\boldsymbol{\Sigma}_k\}$ . The leave-one-out analysis can also be used to calculate the Expect-Log-Probability-Density (Equation 5):

$$\text{ELPD} \equiv \int \mathcal{P}(\mathbf{x}^*) \log \mathcal{P}(\mathbf{x}^* | \mathbf{x}) d\mathbf{x}^* \quad (\text{B40})$$

$$\approx \sum_k \log \mathcal{P}(\mathbf{x}_k | \mathbf{x}_{-k}) \quad (\text{B41})$$

$$= \sum_k \log \mathcal{N}(x_k | x_{\text{loo}_k}, \sigma_{\text{loo}_k}^2) \quad (\text{B42})$$

**Table 6.** Consistency Between HST-Gaia and Radio Masers When Adopting Different ICRS Measurements of SgrA\*

Ref	$\Delta\delta_{\alpha^*}^s$ (mas)	$\Delta\delta_{\delta}^s$ (mas)	$\Delta\mu_{\alpha^*}^s$ (mas yr <sup>-1</sup> )	$\Delta\mu_{\delta}^s$ (mas yr <sup>-1</sup> )
Xu et al. (2022) <sup>a</sup>	-0.536 ± 0.230	-0.517 ± 0.486	-0.076 ± 0.030	-0.042 ± 0.028
Reid & Brunthaler (2020)	-31 ± 10	7 ± 10	-0.072 ± 0.029	-0.043 ± 0.029
Gordon et al. (2023)	-0.368 ± 0.248	0.818 ± 0.457	-0.100 ± 0.051	-0.043 ± 0.080

<sup>a</sup>This is what is adopted throughout the paper.

NOTE—Description of columns.

### C. TRANSFORMING HST-GAIA MEASUREMENTS INTO THE SGRA\*-AT-REST COORDINATE SYSTEM: IMPACT OF DIFFERENT ICRS MEASUREMENTS OF SGRA\*

The ICRS position and proper motion of SgrA\* is required in order to transform the HST-Gaia measurements into a SgrA\*-at-Rest frame (§3.4). Throughout this paper we adopt the ICRS measurements of SgrA\* from Xu et al. (2022), but other recent measurements are available from Reid & Brunthaler (2020)<sup>9</sup> and Gordon et al. (2023)<sup>10</sup>. All three of these studies measure the astrometry of SgrA\* relative to background extragalactic sources via multi-epoch Very Long Baseline Array (VLBA) observations. Reid & Brunthaler (2020) measure the position of SgrA\* relative to two extragalactic sources within 1° of SgrA\*, Xu et al. (2022) by using four nearby extragalactic sources, the same two sources as Reid & Brunthaler (2020) plus two additional sources at larger radii from SgrA\* (~2°), and Gordon et al. (2023) by performing a global fit of the position of SgrA\* using over 1000 extragalactic sources observed across the sky.

Changing the ICRS position and proper motion of SgrA\* can impact the comparison between the HST-Gaia and radio measurements for the stellar masers performed in §4.2.3. Here we repeat the analysis from this section using the SgrA\* ICRS measurements from Reid & Brunthaler (2020) and Gordon et al. (2023) and compare to the results obtained when the Xu et al. (2022) measurement is used. The error-weighted mean differences in the positions and proper motions of the masers and their corresponding uncertainties are shown in Figure 12 and reported in Table 6. In all cases, the HST-Gaia SgrA\*-at-Rest values are consistent with the D23 radio measurements at the 99.7% confidence level, indicating that the HST-Gaia and radio reference frames are consistent in all cases.

The choice of SgrA\* ICRS measurement has little impact on the proper motions, as the proper motions across the studies are consistent within ~0.024 mas yr<sup>-1</sup>. The uncertainty in the Gordon et al. (2023) SgrA\* proper motion is slightly higher than that of Xu et al. (2022) and Reid & Brunthaler (2020), which results in a slightly larger uncertainty in the reference frame. The positions show larger differences, most noticeably with the Reid & Brunthaler (2020) SgrA\* position introducing a ~30 mas offset relative to the other studies, albeit with a large uncertainty. This supports the conclusion that the Reid & Brunthaler (2020) position value is biased due to scatter broadening of radio sources within 1°, where the extragalactic reference sources used in that study are located. Both Xu et al. (2022) and Gordon et al. (2023) establish the position of SgrA\* using reference sources beyond the large scatter broadening region and thus are more accurate. For this paper, we adopt the SgrA\* ICRS position and proper motion from Xu et al. (2022) as it has lower proper motion uncertainties than Gordon et al. (2023) and resolves the position offset from Reid & Brunthaler (2020).

<sup>9</sup> Reid & Brunthaler (2020) measure the ICRS position of SgrA\* to be  $\alpha(\text{J2000}) = 17^{\text{h}}45^{\text{m}}40^{\text{s}}.0409 \pm 0^{\text{s}}.011$  and  $\delta(\text{J2000}) = -29^{\circ}00'28.''118 \pm 0^{\text{s}}.01$  at a reference epoch of 1996.215 (see also Reid & Brunthaler 2004) with a proper motion of  $\mu_{\alpha^*} = -3.156 \pm 0.006$  mas yr<sup>-1</sup>,  $\mu_{\delta} = -5.585 \pm 0.010$  mas yr<sup>-1</sup>.

<sup>10</sup> Gordon et al. (2023) measure the ICRS position of SgrA\* to be  $\alpha(\text{J2000}) = 17^{\text{h}}45^{\text{m}}40^{\text{s}}.034047 \pm 0^{\text{s}}.000018$ ,  $\delta(\text{J2000}) = -29^{\circ}00'28.''21601 \pm 0.''00044$  at a reference epoch of 2015.0 with a proper motion of  $\mu_{\alpha^*} = -3.128 \pm 0.042$  mas yr<sup>-1</sup>,  $\mu_{\delta} = -5.584 \pm 0.075$  mas yr<sup>-1</sup>.

### D. HST-GAIA PROPER MOTION CATALOG IN SGRA\*-AT-REST COORDINATES

For convenience, the catalog of HST-Gaia proper motion measurements that have been transformed into the SgrA\*-at-Rest coordinate system (as discussed in §3.4) is presented in Table 7.

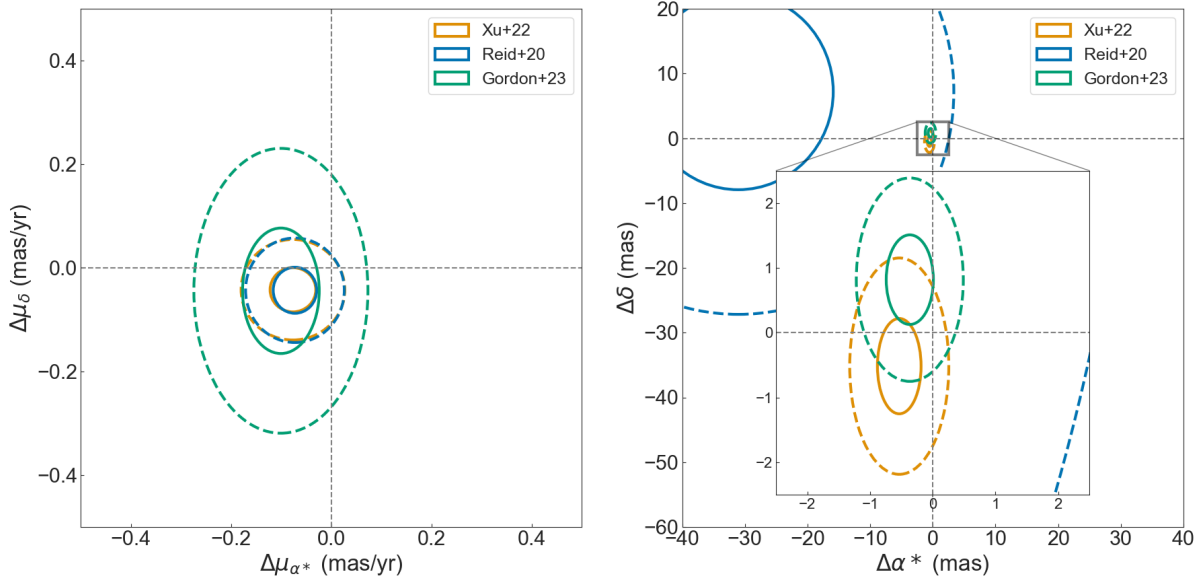


**Figure 12.** The impact of choosing different ICRS positions and proper motions for SgrA\* on the comparison between the HST-Gaia and radio measurements of the stellar masers near SgrA\* (e.g. §4.2.3). The error-weighted mean difference in the maser proper motions (left) and positions (right) are shown using the ICRS SgrA\* values from Xu et al. (2022) (orange), Reid & Brunthaler (2020) (blue), and Gordon et al. (2023) (green). The solid and dashed lines correspond to the 68.3% and 99.7% confidence level of the mean differences, respectively. The Xu et al. (2022) measurement is adopted for this paper, which has the smallest proper motion uncertainties and removes the  $\sim 30$  mas position offset that occurs when the Reid & Brunthaler (2020) measurement is used.

**Table 7.** HST-Gaia Proper Motions: SgrA\*-at-Rest Coordinates

Name	$\delta_{\alpha_0}^s$	$\sigma_{\delta_{\alpha_0}^s}$	$\delta_{\delta_0}^s$	$\sigma_{\delta_{\delta_0}^s}$	$\mu_{\alpha^*}^s$	$\sigma_{\mu_{\alpha^*}^s}$	$\mu_{\delta}^s$	$\sigma_{\mu_{\delta}^s}$	$t_0^s$	Ref Type	Alt Name
	( $''$ )	(mas)	( $''$ )	(mas)	(mas/yr)	(mas/yr)	(mas/yr)	(mas/yr)	(year)		
HST_NSC_007314	0.0137	3.76	-0.2925	3.84	-5.81	0.90	10.05	0.89	2018.4467	0	S0-6
HST_NSC_007079	0.2626	1.01	-0.6155	1.00	8.02	0.25	-5.15	0.25	2015.4906	0	S0-9
HST_NSC_006757	0.5422	0.43	-0.3986	0.42	3.31	0.18	-0.85	0.18	2019.6907	0	S0-13
HST_NSC_007316	-0.5360	5.06	0.4391	1.06	0.90	0.94	2.47	0.30	2019.3942	0	S0-12
HST_NSC_007214	-0.7304	0.40	-0.3036	0.46	2.95	0.08	-1.90	0.10	2018.5698	0	S0-14
HST_NSC_007322	0.3089	1.25	0.8443	1.25	-8.43	0.38	3.00	0.38	2012.8189	0	S1-3
HST_NSC_006751	0.3076	5.72	-0.8739	5.27	-3.40	0.92	4.50	0.88	2013.5218	0	S1-5
HST_NSC_016387	-0.8275	9.01	0.4384	2.66	7.57	1.83	-1.68	0.66	2017.8891	0	S1-26
HST_NSC_007323	1.0858	0.84	0.0458	0.58	5.16	0.16	0.94	0.13	2017.6056	0	S1-1
HST_NSC_006701	0.9668	0.24	0.6109	0.22	-9.44	0.05	7.04	0.04	2018.6155	0	irs16C

NOTE—Description of columns: *Name*: star name,  $\delta_{\alpha_0}^s$ ,  $\delta_{\delta_0}^s$ : star position at  $t_0^s$ ,  $\sigma_{\delta_{\alpha_0}^s}$ ,  $\sigma_{\delta_{\delta_0}^s}$ : star position error at  $t_0^s$ ,  $\mu_{\alpha^*}^{sgrA}$ ,  $\mu_{\delta}^s$ : SgrA\*-at-rest proper motions,  $\sigma_{\mu_{\alpha^*}^s}$ ,  $\sigma_{\mu_{\delta}^s}$ : error in SgrA\*-at-Rest proper motions,  $t_0^s$ : reference epoch of the SgrA\*-at-rest proper motions (calculated as the astrometric-error weighted average time across the epoch dates in Table 1), *Ref Type*: Type of ref star – 0: Secondary reference star, 1: primary reference star, 2: maser, *Alt Name*: Alternative name for star, if applicable (either from Sakai et al. 2019, or Gaia-DR3 catalog)

NOTE—The proper motion fit uncertainties reported in this table ( $\sigma_{\delta_{\alpha_0}^s}$ ,  $\sigma_{\delta_{\delta_0}^s}$ ,  $\sigma_{\mu_{\delta}^s}$ ,  $\sigma_{\mu_{\alpha^*}^s}$ ,  $\sigma_{\mu_{\delta}^s}$ ) do not include the systematic error between the HST-Gaia and the SgrA\*-at-Rest frame discussed in §4.2.2.

NOTE—This table is available in its entirety in the machine-readable format.